JACS
JOURNAL OF THE AMERICAN CHEMICAL SOCIETY
Article
pubs.acs.org/JACS

# Magnetic Circular Dichroism Evidence for an Unusual Electronic Structure of a Tetracarbene–Oxoiron(IV) Complex

Shengfa Ye,[*,†] Claudia Kupper,[‡] Steffen Meyer,[‡] Erik Andris,[§] Rafael Navrátil,[§] Oliver Krahe,[†] Bhaskar Mondal,[†] Mihail Atanasov,[*,†,⊥] Eckhard Bill,[*,†] Jana Roithová,[*,§] Franc Meyer,[*,‡] and Frank Neese[*,†]

[†]Max-Planck Institut für Chemische Energiekonversion, Stiftstr. 34-36, D-45470 Mülheim an der Ruhr, Germany
[‡]Institut für Anorganische Chemie, Georg-August-Universität Göttingen, Tammannstr. 4, D-37077 Göttingen, Germany
[§]Department of Organic Chemistry, Faculty of Science, Charles University in Prague, Hlavova 8, 128 43 Praha 2, Czech Republic
[⊥]Institute of General and Inorganic Chemistry, Bulgarian Academy of Sciences, 1113 Sofia, Bulgaria

Supporting Information

**ABSTRACT:** In biology, high valent oxo–iron(IV) species have been shown to be pivotal intermediates for functionalization of C–H bonds in the catalytic cycles of a range of $O_2$-activating iron enzymes. This work details an electronic-structure investigation of $[Fe^{IV}(O)(L^{NHC})(NCMe)]^{2+}$ ($L^{NHC}$ = 3,9,14,20-tetraaza-1,6,12,17-tetraazoniapenta-cyclohexacosane-1(23),4,6(26),10,12(25),15,17(24),21-octaene, complex **1**) using helium tagging infrared photodissociation (IRPD), absorption, and magnetic circular dichroism (MCD) spectroscopy, coupled with DFT and highly correlated wave function based multireference calculations. The IRPD spectrum of complex **1** reveals the Fe–O stretching vibration at 832 ± 3 $cm^{-1}$. By analyzing the Franck–Condon progression, we can determine the same vibration occurring at 616 ± 10 $cm^{-1}$ in the $E(d_{xy} \rightarrow d_{xz,yz})$ excited state. Both values are similar to those measured for $[Fe^{IV}(O)(TMC)(NCMe)]^{2+}$ (TMC = 1,4,8,11-tetramethyl-1,4,8,11-tetraazacyclotetradecane). The low-temperature MCD spectra of complex **1** exhibit three pseudo *A*-term signals around 12 500, 17 000, and 24 300 $cm^{-1}$. We can unequivocally assign them to the ligand field transitions of $d_{xy} \rightarrow d_{xz,yz}$, $d_{xz,yz} \rightarrow d_{z2}$, and $d_{xz,yz} \rightarrow d_{x2-y2}$, respectively, through direct calculations of MCD spectra and independent determination of the MCD *C*-term signs from the corresponding electron donating and accepting orbitals. In comparison with the corresponding transitions observed for $[Fe^{IV}(O)(SR\text{-}TPA)(NCMe)]^{2+}$ (SR-TPA = tris(3,5-dimethyl-4-methoxypyridyl-2-methy)amine), the excitations within the $(FeO)^{2+}$ core of complex **1** have similar transition energies, whereas the excitation energy for $d_{xz,yz} \rightarrow d_{x2-y2}$ is significantly higher (~12 000 $cm^{-1}$ for $[Fe^{IV}(O)(SR\text{-}TPA)(NCMe)]^{2+}$). Our results thus substantiate that the tetracarbene ligand ($L^{NHC}$) of complex **1** does not significantly affect the bonding in the $(FeO)^{2+}$ unit but strongly destabilizes the $d_{x2-y2}$ orbital to eventually lift it above $d_{z2}$. As a consequence, this unusual electron configuration leads to an unprecedentedly larger quintet–triplet energy separation for complex **1**, which largely rules out the possibility that the H atom transfer reaction may take place on the quintet surface and hence quenches two-state reactivity. The resulting mechanistic implications are discussed.

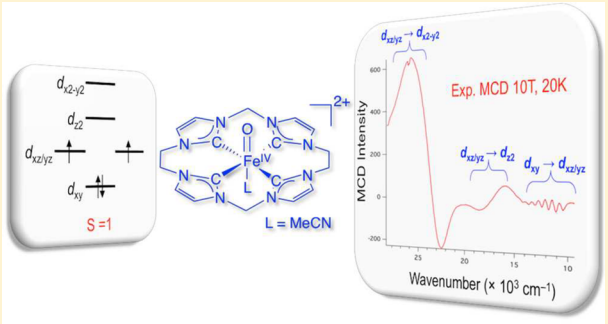


## 1. INTRODUCTION

In the reaction cycle of a range of heme and nonheme iron enzymes, nature couples $O_2$ reduction to functionalization of unactivated C–H bonds.[1] High-valent iron-oxo species have been experimentally identified as pivotal intermediates for this reaction. For cytochrome P450, a prototypical heme enzyme that catalyzes hydroxylation of alkane C–H bonds as a key step in the neutralization of xenobiotics,[2] the intermediate responsible for C–H bond activation is formally a Fe(V) perferryl complex called compound I (P450–I). However, one of the oxidizing equivalents of compound I is located on the macrocyclic ring of the porphyrin ligand, and P450–I is therefore best described as a triplet $Fe^{IV}$oxo unit coupled with a porphyrin anion radical,[1c,3] as deduced first for HRP-I of horseradish peroxidase and later for other heme iron enzyme intermediates.[3c] In contrast, in several nonheme enzymes, the C–H bond cleaving agents have been experimentally authenticated as genuine $Fe^{IV}$oxo species without any ligand radical, having a quintet spin ground state.[4] Below we will make use of the shorthand notation $\Gamma(X)^n$, where $\Gamma$ denotes the bonding nature, X the predominant character of the orbital, and *n* the occupation number, the orbital occupation pattern of a quintet ferryl species in a quasi-octahedral ligand field can be formulated as $\sigma(O\text{-}p_z)^2\pi(O\text{-}p_{x,y})^4NB(Fe\text{-}d_{xy})^1\pi^*(Fe\text{-}d_{xz,yz})^2\sigma^*(Fe\text{-}d_{x2-y2})^1\sigma^*(Fe\text{-}d_{z2})^0$ (NB = nonbonding, Scheme 1b).[5] The

**Received:** July 26, 2016
**Published:** September 28, 2016



DOI: 10.1021/jacs.6b07708
J. Am. Chem. Soc. 2016, 138, 14312–14325

**Scheme 1. Proposed Electronic Configurations for Oxo−Iron(IV) Complexes**

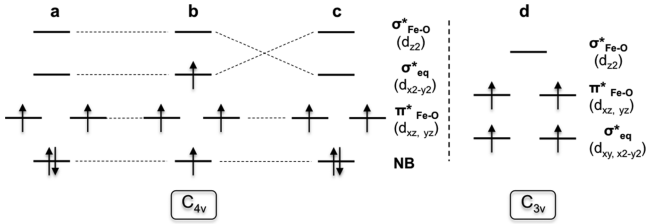


variety of possible modifications of this scheme and the resulting reactivity have triggered synthetic chemists to prepare a wealth of nonheme oxo−iron(IV) model complexes mainly based on polydentate N-donor ligands.[6] The majority of them feature a distorted octahedral coordination geometry and a triplet ground state with an electron configuration of $\sigma(\text{O-p}_z)^2\pi(\text{O-p}_{x,y})^4\text{NB}(\text{Fe-d}_{xy})^2\pi^*(\text{Fe-d}_{xz,yz})^2$ (Scheme 1a). Comparison of the two electron configurations reveals that the energy separation between the NB($\text{Fe-d}_{xy}$) orbital and the $\sigma^*_{eq}(\text{Fe-d}_{x2\text{-}y2})$ orbital has a drastic influence on the ground state spin multiplicity.[7] To the best of our knowledge, only four synthetic six-coordinated oxo−iron(IV) complexes possess a quintet ground state, namely, $[\text{Fe}^{IV}(\text{O})(\text{H}_2\text{O})_5]^{2+}$ [7] and $[\text{Fe}^{IV}(\text{O})(\text{TQA})(\text{X})]^{2+/+}$ (TQA = tris(2-quinolylmethyl)amine, X = NCMe, Cl, Br).[8] For the two systems, employing a weak field ligand ($\text{H}_2\text{O}$) for the former or invoking steric encumbrance for the latter, which causes considerably longer metal−ligand bonds in the equatorial plane, lowers the energy of the $\text{d}_{x2\text{-}y2}$ orbital, thereby favoring the $S = 2$ ground states. On the other hand, supporting ligands having a strong $\sigma$-donating capability may swap the energies of the $\text{d}_{z2}$ and $\text{d}_{x2\text{-}y2}$ orbitals and hence result in a different electron configuration $(\sigma(\text{O-p}_z)^2\pi(\text{O-p}_{x,y})^4\text{NB}(\text{Fe-d}_{xy})^2\pi^*(\text{Fe-d}_{xz,yz})^2$, Scheme 1c). Such a situation was postulated for the triplet ferryl species $[\text{Fe}^{IV}(\text{O})(\text{TAML})]^{2-}$ [9] (TAML = tetraamido macrocyclic ligand) and $[\text{Fe}^{IV}(\text{O})(\text{Porphyrin})]$ (compound II).[10] Furthermore, changing the octahedral coordination environment to a trigonal bipyramid forces the $\text{d}_{xy}$ and $\text{d}_{x2\text{-}y2}$ orbitals to be degenerate and thus also leads to isolation of several quintet oxo−iron(IV) complexes[11] (Scheme 1d).

The reactivity of $\text{Fe}^{IV}$−O species has been studied in some detail and has been found to involve a number of subtleties that require a deep look into the electronic structure of the specific species at hand. Theoretical results predict that, for distorted octahedral oxo−iron(IV) complexes with an $S = 1$ ground state, a low-lying quintet excited state exists and that the triplet oxo−iron(IV) species are more sluggish oxidants toward H atom transfer (HAT) than the corresponding quintet congeners.[12] Recent experimental findings provide strong support for the latter prediction.[13] On the basis of these observations, Shaik and co-workers proposed two-state reactivity to interpret the different reaction rates found for the synthetic triplet ferryl complexes,[14] although recent computational studies suggest that for several ferryl complexes this mechanistic scenario is not operative and the $S = 1$ state is the primary reactive state.[15] In the two-state-reactivity model, the oxo−iron(IV) reactant may presumably first change its spin state from triplet to quintet en route to the transition state for HAT. The subsequent HAT process would thus predominantly occur on the quintet surface. As such, the $\text{Fe}^{III}$−OH product that is generated by HAT processes mediated by triplet oxo−iron(IV) complexes may feature doublet, quartet, or sextet spin states.[12d,g] For the reaction of $[\text{Fe}^{IV}(\text{O})(\text{Bn-TPEN})]^{2+}$ (Bn-TPEN = N-benzyl-N,N′,N′-tris(2-pyridylmethyl)-1,2-diaminoethane) with ethylbenzene, the X-band EPR spectrum recorded at 5 K displays three signals ($g = 2.38$, 2.19 and 1.96), typical of low-spin $\text{Fe}^{III}$, whereas $^1$H NMR Evan's method at room temperature suggests a sextet state.[16] Interestingly, for the reaction of $[\text{Fe}^{IV}(\text{O})(13\text{-TMC})]^{2+}$ (13-TMC = 1,4,7,10-tetramethyl-1,4,7,10-tetraazacyclotridecane) with 1,4-cyclohexadiene, the X-band EPR spectrum at 5 K exhibits two features of $g = 1.96$ and 1.90 in addition to characteristic high-spin $\text{Fe}^{III}$ signals with $g = 7.6$, 6.9, 5.7, 5.3, and 4.3.[17] The above experimental work indicates that the reaction may progress along several channels and hence yields various $\text{Fe}^{III}$ products. This hampers evaluation of the intrinsic HAT reactivity of triplet ferryl species. To this end, a "simple" system that is exempted from the complexity arising from two-state reactivity is highly desired.

Recently, some of us reported an oxo−iron(IV) complex (complex **1** in Scheme 2) supported by a macrocyclic

**Scheme 2. Structures for $[\text{Fe}^{IV}(\text{O})(\text{L}^{NHC})(\text{NCMe})]^{2+}$ ($\text{L}^{NHC}$ = 3,9,14,20-Tetraaza-1,6,12,17-tetraazoniapentacyclohexacosane-1(23),4,6(26),10,12(25),15,17(24),21-octaene, Complex 1)[19] and $[\text{Fe}^{IV}(\text{O})(\text{SR-TPA})(\text{NCMe})]^{2+}$(SR-TPA = tris(3,5-Dimethyl-4-methoxypyridyl-2-methyl)amine, Complex 2)[13,18]**

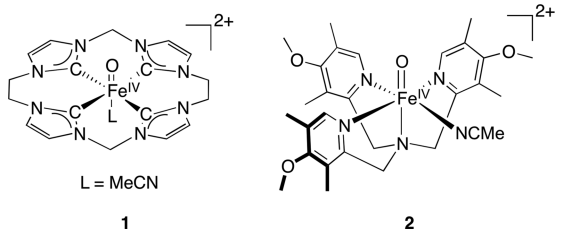


tetracarbene ligand, $\text{L}^{NHC}$.[19] Our DFT calculations indicate that its triplet ground state is stabilized by 18.7 kcal/mol relative to its low-lying quintet state. Clearly, such a wide energy gap suggests that the reaction may not take place on the quintet surface, which makes complex **1** an ideal candidate for a comparative reactivity study. To do so, understanding its different bonding situation compared with the usual triplet ferryl complexes is a prerequisite. Herein, we present a detailed study on the electronic structure of complex **1** by using magnetic circular dichorism (MCD), helium tagging infrared photodissociation (IRPD) spectroscopy in gas phase, and theoretical calculations.

MCD spectroscopy has been widely used to probe electronic structures of transition metal complexes and metalloenzymes.[20] It has been shown that for systems with orbitally nondegenerate ground and excited states, the MCD spectrum is usually dominated by *C*-term transitions, the intensity of which arises from spin−orbit coupling (SOC) between the excited states *J* and *K* (*J*−*K* coupling) or between ground state *A* and excited state *K* (*A*−*K* coupling) (Scheme 3).[21] Nonzero *C*-term intensity gained by the *J*−*K* coupling requires that the electronic transitions $A \rightarrow J$ and $A \rightarrow K$ should be polarized in noncollinear directions that are perpendicular to the SOC vector coupling *J* with *K*. If both transitions can be observed in the MCD spectra, a derivative-shaped band (called a pseudo *A*-term) results because the signs of the two constituent MCD *C*-terms, depending on the symmetry of the states *A*, *J*, *K*, are just


DOI: 10.1021/jacs.6b07708
J. Am. Chem. Soc. 2016, 138, 14312−14325

**Scheme 3. Mechanism for MCD *C*-Term Intensity**

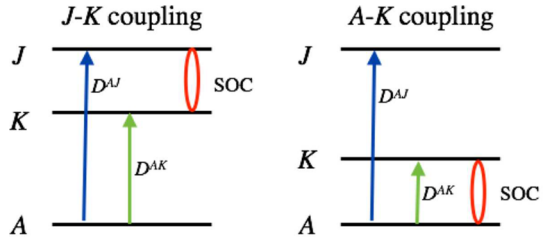


opposite. For a one-electron excitation, the MCD sign can be determined by the symmetry of the electron donating orbital (EDO) and the electron accepting orbital (EAO). To confirm the proposed assignment for a given transition, independently determining its MCD signs is quite crucial. This allows fully exploiting the information content present in MCD spectra and provides more insight into electronic structures. At the same time, it also lowers the possibility of incorrect assignments. However, only a few examples concerning the determination of MCD signs have been reported so far,[22] largely due to the much more complex selection rules for MCD compared to absorption spectroscopy.

The temperature- and field-dependent MCD *C*-term intensity of paramagnetic systems can be simulated by using the following equation:[21a]

$$\frac{\Delta\varepsilon}{E} = \frac{\gamma}{4\pi S}\int_0^{\pi}\int_0^{2\pi}\sum_i N_i(l_x\langle\hat{S}_x\rangle_i M_{yz}^{\mathrm{eff}} + l_y\langle\hat{S}_y\rangle_i M_{zx}^{\mathrm{eff}} + l_z\langle\hat{S}_z\rangle_i M_{xy}^{\mathrm{eff}})\sin\theta\ \mathrm{d}\theta\mathrm{d}\varphi \quad (1)$$

Here, $\frac{\Delta\varepsilon}{E}$ is the MCD intensity, $\gamma$ is a collection of constants, $S$ is the total spin of the ground state, $N_i$ is the Boltzmann population of the $i$th magnetic sublevel of the electronic ground state, $l_{x,y,z}$ are the directional cosine values of the angles between the magnetic field and the molecular coordinate system, and $\langle\hat{S}_{x,y,z}\rangle_i$ are the expectation values of the $x,y,z$ component of the spin operator $\hat{S}$ over the $i$th magnetic eigenstate, respectively. The $M_{vw}^{\mathrm{eff}}$ factors ($v,w = x,y,z$) are effective transition dipole moment products that are fit parameters (eq S3).[21a]

The spin-Hamiltonian (SH) parameters **g**, $D$, and $E$ enter the model through the spin expectation values and the Boltzmann populations of the various magnetic sublevels. Thus, one can determine ground-state SH parameters and the polarizations of the respective electronic transitions through fitting the magnetization curves obtained from variable-temperature variable-field (VTVH) MCD experiments. This method has been successfully applied to analyze MCD spectra of mono-[23] as well as dinuclear transition metal complexes.[24]

The calculation of MCD spectra has been proven to be rather challenging. Perturbational treatments using the formulation of *A*-, *B*-, and *C*-terms (eq S1) have been reported.[25] Recently, linear response perturbation expressions of three MCD terms (eq S1) using time-dependent density functional theory have been worked out by Seth, Ziegler, and co-workers.[26] Although this approach represents definite progress in computing MCD spectra, it only can be applied to the linear response regime with respect to the magnetic field strength. More importantly, because of the intrinsic drawbacks of single determinant methods such as density functional theory, multiplet effects and double excitations that prevail in the optical spectra of transition metal complexes cannot be properly described. To avoid the limitations of the linear response theory and to circumvent the problems arising from multiplet effects and double excitations, multireference approaches[27] such as the complete active space self-consistent field (CASSCF)[28] and second-order *N*-electron valence perturbation theory (NEVPT2)[29] are methods of choice. Exact diagonalization is employed to directly compute the difference between transition probabilities for left- and right-circular polarized light in the presence of a homogeneous external magnetic field. Specifically, we first calculate ground- and excited-state wave functions using quasi-degenerate perturbation theory (QDPT), which explicitly accounts for SOC, spin−spin coupling (SSC), and Zeeman interactions, and then based on the resulting relativistic wave functions transition energies and intensities for LCP and RCP light are estimated.[30a] The approach was tested successfully for diatomic molecules as well as for transition metal complexes.[30]

## 2. MATERIALS AND METHODS

**2.1. Magnetic Circular Dichroism (MCD) and Absorption Spectroscopy.** MCD samples of complex **1** (triflate salt)[19] were prepared as 1.63 mM solution in butyronitrile. Upon freezing, the solvent formed a transparent glass with a minor number of cracks, which made it suitable for MCD measurement. The solutions were transferred to precooled MCD holders with precooled syringes and then frozen in liquid nitrogen. A different solvent (acetonitrile) was used for preparing samples for other spectroscopic studies (vide infra) because butyronitrile is a better glassing solvent with which transparent frozen solutions required for MCD investigations can be easily obtained.

MCD experiments were carried out with an Olis DSM17 CD spectrapolarimeter with the energy varied from 5000 $cm^{-1}$ (2000 nm) to 30 000 $cm^{-1}$ (333 nm); the sample was placed in an Oxford cryostat Spectromag SM4000 with the temperature ranging from 2−80 K. Electronic absorption spectra were also recorded on the same sample with the Olis DSM17 instrument from 20−80 K as well as on the sample from independent preparations at 293 K with a Varian Cary 5000 instrument (Agilent Technologies). Acetonitrile solutions were prepared in quartz cuvettes (1 cm path length) in two concentrations; $1.5 \times 10^{-4}$ and $4 \times 10^{-3}$ mM. Global fits of MCD and absorption spectra of consistent temperature and field series with Gaussian lines were performed with an in-house program (mcd_bf). Line positions were kept identical throughout the series, whereas line widths were allowed to vary as a function of temperature by 10−20%; intensities have been released unconstrained except for pseudo-*A* term signals.

At the peak positions, we carried out VTVH MCD experiments in which the MCD intensity was measured at the fixed wavelength as a function of temperature and magnetic field. The results are presented as isothermal plots of MCD intensity versus $\mu_B B/kT$, where $\mu_B$ is the Bohr magneton, $k$ is Boltzmann constant, $B$ is strength of the magnetic induction, and $T$ is absolute temperature. The VTVH magnetization curves, which showed a pronounced nesting behavior as expected for MCD *C*-term signals from $S > 1/2$ systems, have been simulated by using our program mcd3D_S for global fits, based on eq 1. Besides the intensity variations of the experimental spectra at distinct wavelengths, the intensity variation of a given transition derived from global spectra simulations has also been analyzed in the same manner. From the fitted effective transition dipole moments factors, $M_{vw}^{\mathrm{eff}}$, for


DOI: 10.1021/jacs.6b07708
J. Am. Chem. Soc. 2016, 138, 14312−14325

these bands, their individual polarizations have been calculated by using the relation

$$\%x = 100 \times \frac{(M_{xy}^{\mathrm{eff}} \times M_{xz}^{\mathrm{eff}})^2}{(M_{xy}^{\mathrm{eff}} \times M_{xz}^{\mathrm{eff}})^2 + (M_{xy}^{\mathrm{eff}} \times M_{yz}^{\mathrm{eff}})^2 + (M_{xz}^{\mathrm{eff}} \times M_{yz}^{\mathrm{eff}})^2} \quad (2)$$

for the percentage of *x*-polarization, and its permutations to obtain the corresponding *y*- and *z*-components of the polarization.[21a]

**2.2. Helium Tagging Infrared Photodissociation (IRPD) Spectroscopy.** IRPD spectra were measured with the ISORI instrument described in detail in ref 31. For the preparation of complex **1**, $[Fe(L^{NHC})(NCMe)_2]^{2+}$ (1.9 mg of the triflate salt) and 2-iodosylphenyl *tert*-butyl sulfone (3 mg, ~2.8 equiv) were charged to a flask cooled by liquid nitrogen. Then 3 mL of acetonitrile was added, and the mixture was slowly warmed to −40 °C while stirring until all components were dissolved. The solution was transferred to a syringe operating at −10 °C and introduced via a silica capillary to the mass spectrometer. $^{18}O$ labeled complex **1** was prepared in the same way with addition of 8 μL of $H_2{}^{18}O$ to 400 μL of the acetonitrile solution. The electrospray ion source was kept at room temperature, and soft ionization conditions were used. The $[Fe^{IV}(O)(L^{NHC})(NCMe)]^{2+}$ ions were mass selected (*m*/*z* 230.5) by the first quadrupole and transferred with an octopole toward a cryo-cooled wire quadrupole ion trap operated at 3 K and 1 Hz. The ions were introduced to the trap during the first 200 ms and trapped with a helium buffer gas pulse (130 ms long). About 15% of the trapped ions were transformed to the helium tagged complexes, $[Fe^{IV}(O)(L^{NHC})(NCMe)(He)]^{2+}$ (*m*/*z* 232.5). After a 400 ms time delay, the ion cloud was irradiated by eight photon pulses generated in an optical parametric oscillator/amplifier (OPO/OPA) operating at 10 Hz frequency. At 990 ms, the exit electrode of the trap was opened, the ions were mass-analyzed by the second quadrupole, and their number (*N*) was determined by a Daly type detector operated in ion-counting mode. In the following cycle, the light from the OPO was blocked by a mechanical shutter, giving the number of unirradiated ions ($N_0$). The IRPD spectra are constructed as the wavenumber dependence of $(1 - N/N_0)$. The calibration was done using the absorption of methane and water (see Figure S6 in the Supporting Information); the positions of the bands are determined with accuracy better than ±3 $cm^{-1}$.

**2.3. Computational Setup.** All calculations were performed with the ORCA program package.[32] Ground-state geometry optimizations and frequency calculations were carried out by using the BP86 density functional[33] along with the semiempirical van der Waals corrections due to Grimme.[34] Def2-TZVP(−f)[35] basis sets on all atoms were used. The density fitting and "chain of spheres" (RIJCOSX)[36] approximations were employed to accelerate the calculations in conjunction with the auxiliary basis sets def2-TZV/J.[37] Solvation effects were taken into account by using the conductor-like screening model (COSMO),[38] for which acetonitrile was selected as the solvent in the calculations. Excited-state geometry optimizations and frequency calculations for $^3E(d_{xy} \rightarrow d_{xz,yz})$ were performed by employing time-dependent DFT theory[39] with the BP86 density functional.

The CASSCF/NEVPT2 approach was used to compute the MCD spectra of complex **1**. In the CASSCF calculations, an active space consisting of 12 electrons in the five Fe-3d based molecular orbitals (MOs), the three oxo-p orbitals, and the bonding counterpart of the Fe-$d_{x2-y2}$ orbital (CAS(12,9)) was chosen. CASSCF is designed to mainly capture static correlation energies and hence lacks balanced treatments between static and dynamic correlation effects. By using NEVPT2, dynamic correlation effects were explicitly introduced. The CASSCF results erroneously predict a quintet ground state for $[Fe^{IV}(O)(SR\text{-}TPA)(NCMe)]^{2+}$ (SR-TPA = tris(3,5-dimethyl-4-methoxypyridyl-2-methyl)amine, complex **2** in Scheme 2).[40] This is akin to the strong bias of Hartree−Fock-type self-consistent field treatments for high-spin states. Since the NEVPT2 calculations deliver the correct spin-state energetics, we will only discuss the NEVPT2 results in the following.

Additional insight into the iron-ligand bonding in complexes **1** and **2** is obtained by subjecting the CASSCF/NEVPT2 results to the recently developed ab intio ligand field theory (AILFT) analysis.[41] In the first step, state-averaged CASSCF (5 *S* = 2 and 45 *S* = 1 multiplets) calculations with four electrons distributed over the minimal active space of five Fe-3d centered MOs were carried out. Then a least-square fit of the matrix elements of the 5 × 5 ligand field matrix and the Racah parameters of interelectronic repulsion B and C to the numerical data from the CASSCF/NEVPT2 results allows determination of these parameters. The 5 × 5 ligand field matrices can then be interpreted by using the angular overlap model, which yields the parameters of the metal−ligand antibonding interaction for complexes **1** and **2** (see the Supporting Information for more details).

## 3. RESULTS AND DISCUSSION

**3.1. Absorption and MCD Spectra.** The absorption spectrum of complex **1** in a butyronitrile solution shows a distinct broad band in the visible region around 26 000 $cm^{-1}$ ($\varepsilon \approx 1100$ $M^{-1}$ $cm^{-1}$) and two weaker near-IR absorptions at about 16 500 $cm^{-1}$ ($\varepsilon \approx 160$ $M^{-1}$ $cm^{-1}$) and 12 000 $cm^{-1}$ ($\varepsilon \approx 30$ $M^{-1}$ $cm^{-1}$) (Figure 1A). These three features give rise to rich MCD spectra with enhanced resolution for the partially overlapping transitions. At low temperature, 1.9 K, and strong field, 10 T, the experimental MCD spectrum exhibits positive bands at about 26 000, 19 500, 16 240 $cm^{-1}$, and a weak negative dip at 22 600 $cm^{-1}$ (Figure 1C). Remarkably, a transition with strikingly resolved vibrational progressions is found in the MCD spectra around 11 500 $cm^{-1}$. Each vibronic transition appears to be of a Gaussian derivative band shape, as expected for MCD *A*-term excitations, but its intensity is field and temperature dependent like those of the other MCD bands, thereby clearly indicating that a *C*-term mechanism is operative. On the basis of the corresponding VTVH measurements performed at a whole range of distinct experimental wavelengths shown in Figures 2 and S1, we conclude that the lowest-energy transition observed in the MCD spectrum is a pseudo *A*-term signal, arising from two related, overlapping *C*-term transitions of opposite sign. The presence of another pseudo *A*-term transition around 17 000 $cm^{-1}$ can be easily inferred from the apparent shift of the peak maximum in that region found at elevated temperatures (Figure 1B). Apparently, the positive transition at 16240 $cm^{-1}$ is superimposed with a negative pseudo *A*-term signal. (The sign of a pseudo *A*-term is defined as that of the higher energy *C*-term transition.) In addition, at higher temperatures, a strong negative band at about 22 600 $cm^{-1}$ develops. Compared to over 40 well-characterized *S* = 1 oxo−iron(IV) complexes reported thus


DOI: 10.1021/jacs.6b07708
J. Am. Chem. Soc. 2016, 138, 14312−14325

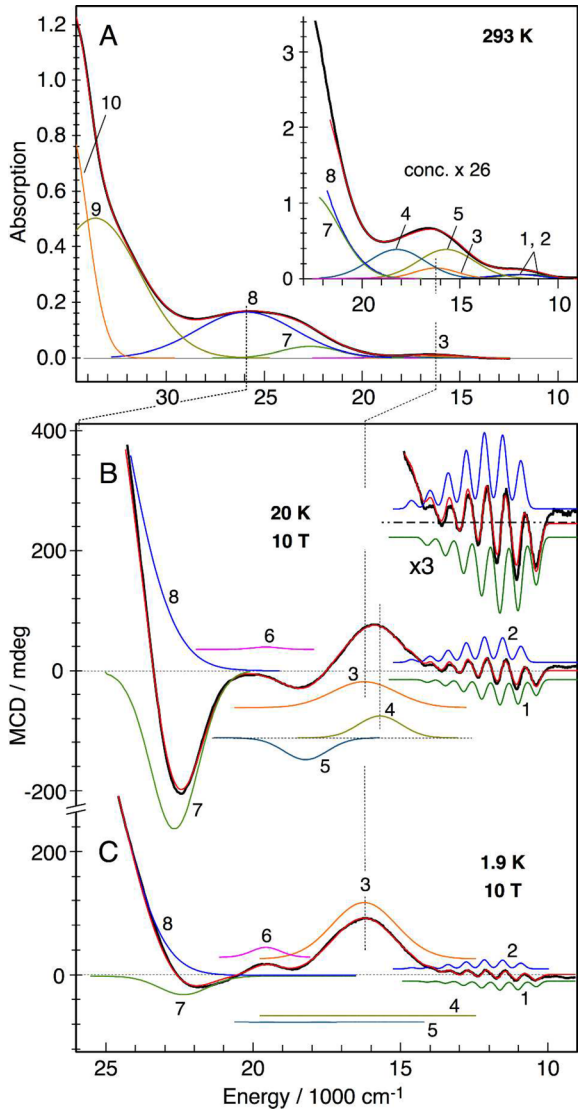


**Figure 1.** Electronic absorption and low-temperature MCD spectra of complex **1**, measured in a fluid acetonitrile solution at 293 K (A) and in a frozen butyronitrile solution at 1.9 and 20 K with 10 T applied field, respectively (B, C). Experimental data are shown in black. The red lines are the result of a global simulation with bands 1−8 (parameters summarized in Table 1). Two additional bands, 9 and 10, have been adopted for simulating the high-energy region of the absorption spectrum with the excitation energies of 33 620 and 35 000 $cm^{-1}$ and the line widths of 4540 and 2400 $cm^{-1}$, respectively. The inset in panel B shows a 3× zoom of the low-energy region together with the baseline (dashed-dotted line) to better visualize the superposition of the two $^3E$ transitions, bands 1 and 2, having opposite MCD signs.

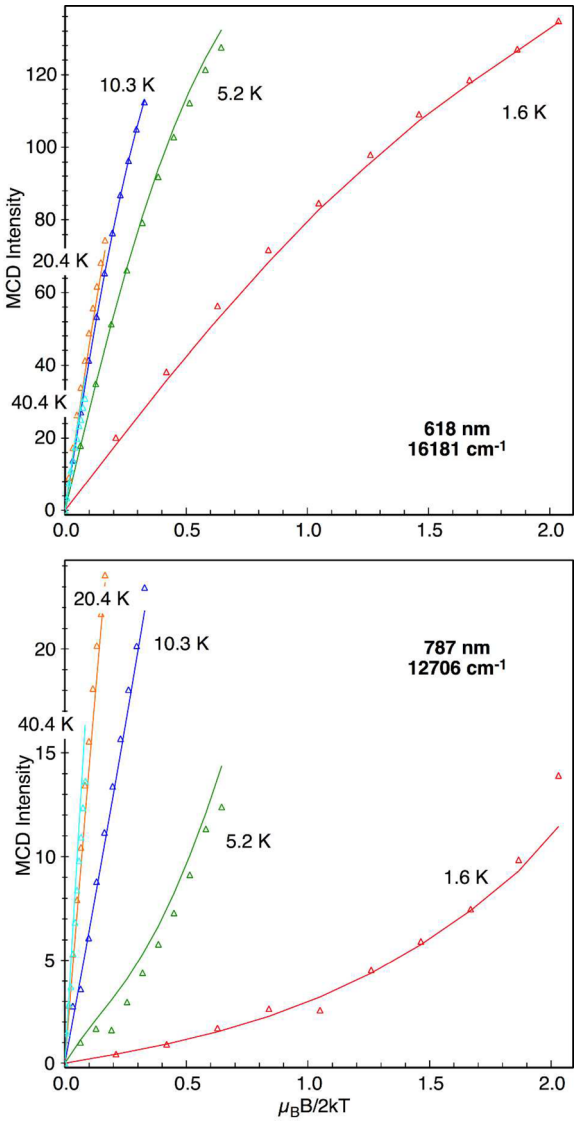


**Figure 2.** MCD VTVH intensity data for complex **1** recorded at 618 and 787 nm and five indicated temperatures with the field swept from 0−10 T (symbols). The lines are spin Hamiltonian simulations for $S$ = 1 using eq 1 with $D$ = 17.4 $cm^{-1}$, $E/D$ = 0.08, $g$ = (2.2, 2.2, 1.98), and $M_{ij}$ factors (1.3, 1.3, −0.25) for 618 nm and (0.24, 0.24, 10.8) for 787 nm.

far,[6c] which typically exhibit a broad ligand field band in the energy range of 12 000−14 000 $cm^{-1}$, complex **1** features two discernible d−d bands with the intense one appearing at a considerably higher energy (~17 000 $cm^{-1}$). Interestingly, for the corresponding MCD transitions, the sign of the pseudo *A*-term signal observed for complex **1** is just opposite to that for complex **2**[40] and related triplet ferryl species.[42]

The interpretation of the MCD spectra could be achieved via a quantitative Gaussian deconvolution by using a unique minimal set of eight bands with the same energies and line widths for all temperatures and fields, but varying intensities. For demonstration, a whole temperature series of spectra recorded in the range of 1.9−80 K is shown in Figure S1. More importantly, the absorption spectrum recorded at 300 K was also included in the global fit with absorption line shapes, for which up to 20% line broadening was allowed for the higher temperature. The deconvoluted MCD and absorption spectra shown in Figure 1 contain eight bands, 1−8 as depicted in different colors with offsets for the MCD spectra. Two additional intense broad bands (9 and 10) are required to fit the high-energy feature of the absorption spectrum. On the basis of their intensities, one can safely assign them as charge transfer (CT) transitions. The fitting parameters are summarized in Table 1 and the caption of Figure 1. The large $C_0/D_0$ values (>0.5), the ratios between MCD and absorption intensities, indicate that bands 1−8 are all mainly d−d transitions in nature.



DOI: 10.1021/jacs.6b07708
J. Am. Chem. Soc. 2016, 138, 14312−14325

Table 1. Simulation Parameters Obtained from Simultaneous Gaussian Fits of the Absorption and MCD Spectra of Complex 1

| band | energy exp. ($cm^{-1}$) | line width ($cm^{-1}$) | $C_0/D_0$ | dipole products $M_{yz}$, $M_{xz}$, $M_{xy}$ | % polarization ($x$,$y$,$z$) | energy calc. ($cm^{-1}$) | assignment[b] |
|---|---|---|---|---|---|---|---|
| 1 | 12 410[a] | 270 | 21.7 | 0, 0, 5.5 | 50, 50, 0 | 13 100 | $^3E(1b_2 \rightarrow 2e)$ $d_{xy} \rightarrow d_{xz,yz}$ |
| 2 | 12 930[a] | 270 | 21.7 | 0, 0, −3.7 | 50, 50, 0 | 13 200 | $^3E(1b_2 \rightarrow 2e)$ $d_{xy} \rightarrow d_{xz,yz}$ |
| 3 | 16 240 | 1473 | 6.5 | 0.6, 0.6, −8.9 | 45, 45, 10 | 23 700 | $^3A_2(1b_2 \rightarrow 2a_1, 2b_1)$ $d_{xy} \rightarrow d_{z2,x2-y2}$ |
| 4 | 15 700 | 2181 | 3.4 | 0.9, 0.9, −2 | 50, 50, 0 | 18 820 | $^3E(2e \rightarrow 2a_1)$ $d_{xz,yz} \rightarrow d_{z2}$ |
| 5 | 18 220 | 1473 | 3.4 | −0.5, −0.5, 6.9 | 50, 50, 0 | 18 860 | $^3E(2e \rightarrow 2a_1)$ $d_{xz,yz} \rightarrow d_{z2}$ |
| 6 | 19 570 | 996 | 0.5 | 1.0, 1.0, −4.3 | 48, 48, 4 | 24 460 | $^3A_2(1b_2 \rightarrow 2a_1, 2b_1)$ $d_{xy} \rightarrow d_{z2,x2-y2}$ |
| 7 | 22 660 | 1670 | 3.0 | −0.4, −0.4, 13 | 50, 50, 0 | 25 010 | $^3E(2e \rightarrow 2b_1)$ $d_{xz,yz} \rightarrow d_{x2-y2}$ |
| 8 | 25 920 | 3121 | 2.0 | 1.0, 1.0, 5.7 | 49, 49, 2 | 25 160 | $^3E(2e \rightarrow 2b_1)$ $d_{xz,yz} \rightarrow d_{x2-y2}$ |

[a]For comparison with the computed vertical excitation energies, the transition energies at maximum intensity of the Franck−Condon progressions found for band 1 and 2 are listed. The energies of the corresponding 0−0 lines for bands 1 and 2 are 10 400 and 10 920 $cm^{-1}$, respectively (see section 3.2 and Figure S2). The vibrational splitting of the progression for both bands was found to be 616 ± 15 $cm^{-1}$, and the intensity distributions of the progression lines were characterized by a common Huang−Rhys factor $S_{HR}$ = 3.1. [b]Symmetries of excited states and the orbitals involved in electronic transitions are labeled according to the irreducible representations of the effective $C_{4v}$ point group (vide infra). Distortions to lower ($C_s$) symmetry induce a splitting of each $^3E$ state into two sublevels (see Tables S1 and S2 in the Supporting Information.)

Examples of the experimental VTVH MCD magnetization curves of complex **1** are presented in Figure 2 for the prominent NIR bands seen at 12 700 $cm^{-1}$ (787 nm) and 16 180 $cm^{-1}$ (618 nm). The data (dots) were recorded at 1.5, 5, 10, 20, and 40 K with the magnetic field varying from 0 to 10 T. As expected, these isotherms show significant nesting behavior, in accord with the substantial zero-field splitting (ZFS) expected for the $3d^4$, $S$ = 1 configuration. The solid lines represent the best global SH simulation obtained with parameters $D$ = 17.4 $cm^{-1}$, $E/D$ = 0.08, $g$ = (2.2, 2.2, 1.98) by using eq 1; the corresponding transition dipole products $M_{ij}$ are given in the caption. The latter, however, have to be considered as "effective" values without much physical meaning because the contributions from several transitions, particularly of opposite signs, are overlapping at the wavelengths selected for the experimental intensity measurements. In contrast, the resulting SH parameters are globally valid and unique. Their values fit nicely to those obtained previously for **1** measured in solid state by using magnetic susceptibility data and magnetic Mössbauer spectroscopy, which yielded $D$ = 16.8 $cm^{-1}$, and 15(2) $cm^{-1}$, respectively (with $E/D$ = 0.08, $\langle g \rangle$ = 1.9).[19]

Since the effective transition dipole products $M_{yz}$, $M_{xz}$, $M_{xy}$ obtained from the experimental VTVH scans (Figure 2) cannot be directly related with the polarization property of any individual transition due to the severe overlap of bands, we deduced the polarization parameters of a given transition from its intensity variation with the temperature varied from 2−80 K (Figure S1) in the 10 T MCD spectra (Figure 1). A global SH analysis with the parameters $D$ = 17.4 $cm^{-1}$, $E/D$ = 0.08, $g$ = (2.2, 2.2, 1.98) as given above yielded the individual VTVH curves for all bands 1−8 shown in Figure 3. According to the resulting $M_{ij}$ products, we computed the fractional polarization factors for all bands by using eq 2 and summarized them in Table 1.

**3.2. Vibrational Properties.** Following the route which Solomon and co-workers have employed to study the vibronic structures found for the related ferryl complexes,[42] we performed a similar Franck−Condon analysis of the nicely resolved vibronic progression observed for bands 1 and 2. According to our electronic-structure analysis, both transitions can be unequivocally assigned to the $d_{xy} \rightarrow d_{xz,yz}$ ligand field transitions (vide infra) so that the average spacing of the progression should essentially represent the Fe−O stretching frequency of complex **1** in the excited state. In this picture, the excitation of an electron from the NB $d_{xy}$ orbital to a $\pi$-antibonding $d_{xz,yz}$ orbital weakens and elongates the Fe−O bond in the excited state by a fraction $\Delta r$. More importantly, the excitation also reduces the force constant $k$ for the Fe−O stretching mode, which leads to a weaker vibration energy $h\nu_{es}$ in the excited state than that in the ground state ($h\nu_{gs}$). Because of the distinct equilibrium geometries between the ground and excited states, the excited-state energy at the ground-state equilibrium geometry of the Fe−O unit is higher than its minimum by $1/2k_{es}\Delta r^2$. The intensity distribution of the $n$th progression lines of bands 1 and 2 can be fitted with the Poisson distribution,

$$\frac{I_{0-n}}{I_{0-0}} = \frac{S_{HR}{}^n}{n!} \tag{3}$$

in which $I_{0-0}$ and $I_{0-n}$ are the intensities of the 0−0 and 0−$n$ vibronic transitions (exp. lines), and $S_{HR}$ is the Huang−Rhys factor that measures the distortion of the excited-state potential energy surface relative to that of the ground state:

$$S_{HR} = \frac{\frac{1}{2}k_{es}\Delta r^2}{h\nu_{es}} \tag{4}$$

We investigated different possibilities for the positions of the 0−0 lines at which our band shape simulations can start. It turns out that the best fit can only be achieved by assigning the 0−0 transition to the first, well resolved lines in the experimental traces. Poisson distributions starting at lower energies yielded clearly worse fits with significant deviations from the experiment, as exemplified in Figure S2 for the spectrum recorded at 20 K with 10 T field (the best fit is depicted in Figure 1B).

The average energy separation of the progression lines obtained from the simulations is $h\nu_{es}$ = 616 ± 15 $cm^{-1}$ corresponding to the energy of the Fe−O stretching vibration in the excited state. As expected, this value is considerably lower than that measured for the ground state of complex **1** (vide infra).

**3.3. Infrared Photodissociation Spectroscopy.** The IR spectrum of the ground-state complex has been obtained experimentally by helium tagging infrared photodissociation (IRPD) spectroscopy.[43] The $[Fe^{IV}(O)(L^{NHC})(NCMe)]^{2+}$ ions were generated from an acetonitrile solution by electrospray ionization, mass-selected and transferred to an ion trap



DOI: 10.1021/jacs.6b07708
J. Am. Chem. Soc. 2016, 138, 14312−14325

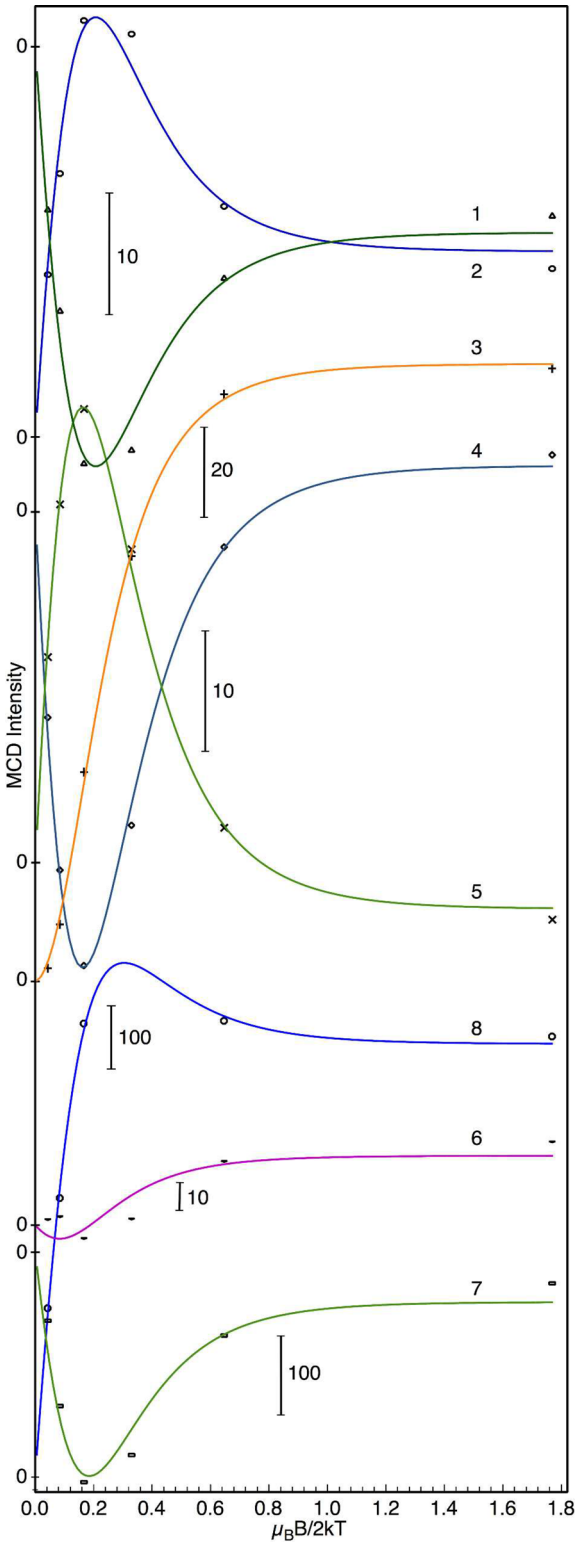


**Figure 3.** Global SH simulation of the temperature dependence of bands 1−8 found for complex **1** with 10 T applied field. The band intensities (dots) have been obtained by global band fitting of the corresponding (complete) MCD spectra recorded at 10 T instead of recording experimental single-point data. Therefore, the band overlap is properly considered by this procedure (energies and bandwidth have been kept constant, Table 1). The curves are calculated with a unique common set of the optimized SH parameters for the ground state, $D$ = 17.4 $cm^{-1}$, $E/D$ = 0.08, $g$ = (2.2, 2.2, 1.98), and the independent transition dipole products $M_{ij}$ for each transition are given in Table 1.

operating at 3 K. The internal energy of the ions in the trap is so low that they form weakly bound complexes with present helium atoms. Subsequent absorption of an IR photon leads to an increase of internal energy and thus to the dissociation of the helium complexes. Mass spectrometric monitoring of the elimination of helium atoms provides a very sensitive way of recording of an IR photon absorption. Hence, IR spectra were obtained as photon-energy dependent monitoring of helium elimination from the $[Fe^{IV}(O)(L^{NHC})(NCMe)(He)]^{2+}$ complexes. We have determined that the ground state Fe−O stretching vibration of the complex **1** is at 832 ± 3 $cm^{-1}$ (Figure 4). $^{18}O$ labeling leads to a red shift of the Fe−O band

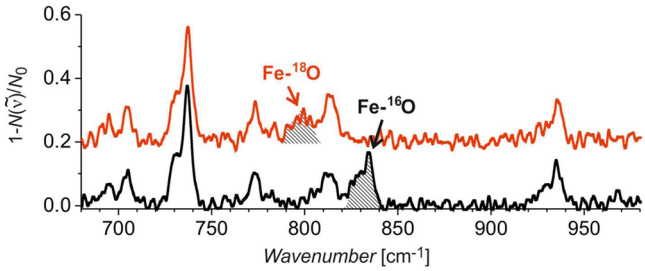


**Figure 4.** Helium tagging IRPD spectrum of $[Fe^{IV}(^{16}O)(L^{NHC})(NCMe)]^{2+}$ (black line) and its $^{18}O$-labeled isotopomer (red line).

to 799 ± 3 $cm^{-1}$ (the $^{18}O$-labeled complex was prepared by oxygen exchange between the complex and $H_2{}^{18}O$ in solution). The computed Fe−O stretching frequency (840 $cm^{-1}$) and its $^{18}O$ isotope shift (36 $cm^{-1}$) with the BP86 density functional are in good agreement with the experimental values, further corroborating our assignment. The Fe−O stretching frequency detected for complex **1** is very similar to those reported for other $S$ = 1 oxo−iron(IV) complexes, which are mostly found in the range of 815−855 $cm^{-1}$.[6c] Specifically, the closely related cyclam-based complex with a MeCN ligand *trans* to the Fe=O unit, $[Fe^{IV}(O)(TMC)(NCMe)]^{2+}$ (TMC = 1,4,8,11-tetramethyl-1,4,8,11-tetraazacyclotetradecane), features its Fe−O stretch at 839 $cm^{-1}$.[44]

**3.4. Electronic Structure.** In comparison with oxo−iron(IV) complexes supported by N-donor ligands, our calculations propose a distinct electron configuration for complex **1** (Figure 5) with an orbital occupation pattern as sketched in Scheme 1, panel c versus the usually adopted one shown in Scheme 1, panel a. However, to the best of our knowledge, no solid evidence has been put forward to prove this theoretical prediction of the bonding model (Scheme 1c). The difficulty lies in the fact that for both configurations a and c in Scheme 1, the Fe-$d_{z2}$ and -$d_{x2-y2}$ orbitals are vacant and hence cannot be readily probed by ground state methods such as Mössbauer and EPR spectroscopy. To gain detailed information about them, one must resort to the spectroscopy of electronically excited states to investigate the related ligand field transitions. Prior to delving into interpretation of the spectroscopic properties of complex **1**, we first enumerate the low-energy d−d excitations (Figure 5). The important single excitations within the metal d-shell are those from the $1b_2$(Fe-$d_{xy}$) orbital to the singly occupied nearly degenerate 2e(Fe-$d_{xz,yz}$)-set, from which the excited state of $^3E(1b_2 \rightarrow 2e)$ symmetry arises. Similarly, the excitations 2e(Fe-$d_{xz,yz}$) → $2a_1$(Fe-$d_{z2}$), $2b_1$(Fe-$d_{x2-y2}$) give rise to the excited states $^3E(2e \rightarrow 2a_1)$ and $^3E(2e \rightarrow 2b_1)$. Promotion of one electron from the $1b_2$(Fe-$d_{xy}$) orbital to $2a_1$(Fe-$d_{z2}$) and $2b_1$(Fe-$d_{x2-y2}$) leads to a


DOI: 10.1021/jacs.6b07708
J. Am. Chem. Soc. 2016, 138, 14312−14325

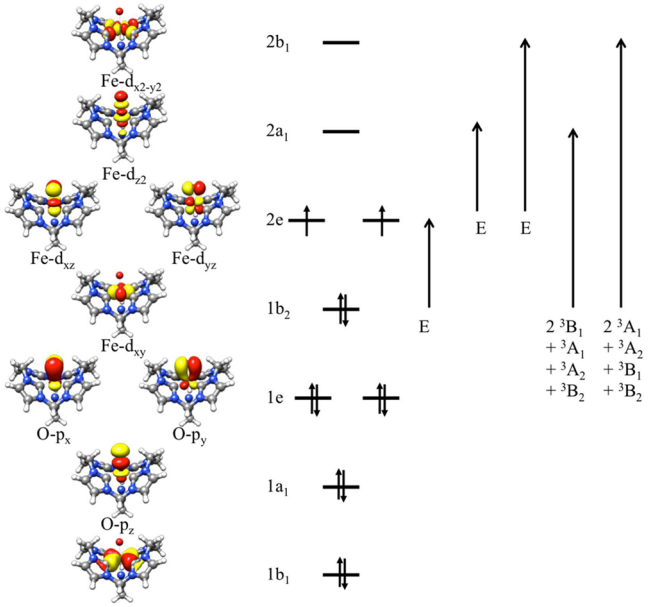


**Figure 5.** CASSCF active orbitals of complex **1** and the spin-allowed d−d excitations. The indicated orbital occupation pattern corresponds to the $^3A_2$ ground state under the effective symmetry of $C_{4v}$. Note that the position of the orbital on the left-hand side does not reflect its relative energy; hence, the length of the arrow denoting a given transition does not represent its relative energy.

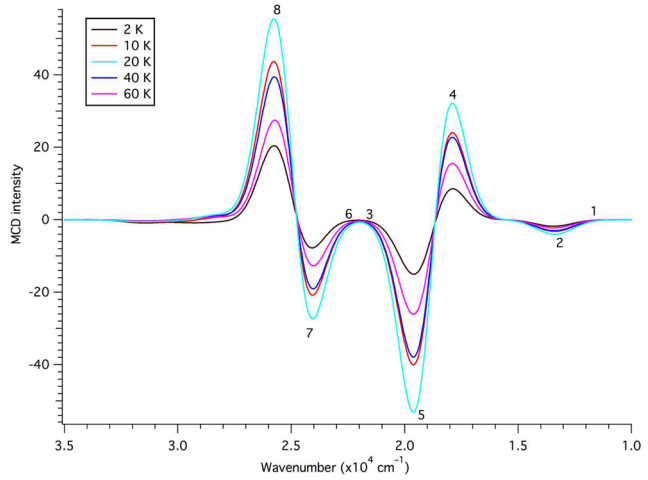


**Figure 6.** Computed MCD spectra of complex **1** at 10 T and indicated temperatures. To simulate unresolved line broadening, Gaussian bands with the full-width-half-maximum of 2000 cm$^{-1}$ were employed.

range of excited states because the number of unpaired electrons increases from two to four, hence inducing complex multiplet effects and spin-coupling patterns (Scheme S2). If the spin of the two electrons residing in the 2e-set is parallel, the excited states are of $^3B_1(1b_2 \rightarrow 2a_1)$ ( × 2) and $^3A_1(1b_2 \rightarrow 2b_1)$ ( × 2) symmetry. Conversely, if the spin of the 2e-electrons is antiparallel, excited states of $^3A_1(1b_2 \rightarrow 2a_1)$, $^3A_2(1b_2 \rightarrow 2a_1)$, $^3B_1(1b_2 \rightarrow 2a_1)$ symmetries and of $^3A_2(1b_2 \rightarrow 2b_1)$, $^3B_1(1b_2 \rightarrow 2b_1)$, $^3B_2(1b_2 \rightarrow 2b_1)$ symmetries arise, respectively.

**3.5. Assignment.** Time-dependent DFT calculations based on single Kohn−Sham determinants qualitatively fail in calculating the transitions of the type $1b_2 \rightarrow 2a_1$ and $1b_2 \rightarrow 2b_1$ because only two excited states for each excitation can be obtained rather than five as analyzed above. Therefore, we employed multireference CASSCF approaches to compute MCD spectra, and final transition energies were corrected by using the NEVPT2 theory. In our earlier work,[40] this method has been used to compute the MCD spectra of complex **2** and found to deliver reasonably accurate transition energies and intensities. As shown in Table 1, our calculations nicely reproduce the transition energies of most ligand field transitions with an error of ∼3000 cm$^{-1}$ and their temperature-dependent intensity variations (Figure 6). The errors fall within the well-accepted uncertainty range of state-of-the-art wave function based quantum chemical approaches. Furthermore, because in MCD spectroscopy the differential absorption ($\Delta\varepsilon$) between the left (LCP) and right (RCP) circular polarized light of a sample is measured, the peaks in MCD spectra do not necessarily reflect the vertical transition energies, especially for two transitions with similar excitation energies but opposite in signs. This may explain the larger energy separation found for the two nearly degenerate components of the $E(d_{xz,yz} \rightarrow d_{z2})$ (bands 4 and 5) and $E(d_{xz,yz} \rightarrow d_{x2-y2})$ states (bands 7 and 8). However, the excitation energies for bands 3 and 6 were considerably overestimated for reasons that will be discussed below. In addition, our CASSCF/NEVPT2 calculations predict the dipole allowed ligand-to-metal charge transfer (LMCT) excitations from the O-$p_{x,y}$ orbitals to Fe-$d_{xz,yz}$ to occur at energies above 35 000 cm$^{-1}$, far beyond the transition energies measured for bands 9 and 10. This is due to the fact that CT transitions are always accompanied by substantial differential radial electron correlation arising from the considerable change in the radius of the metal center during CT processes.[45] Our employed active space is not flexible enough to properly describe this effect. To accurately account for the resulting electronic relaxation, the active space would have to be enlarged to include metal double d-shells,[46] which would render conventional CASSCF calculations impossible. The second layer of complexity necessary to achieve unequivocal assignments for bands 9 and 10 comes from the possibility that they may be the LMCT transitions from the supporting carbene ligand. In the following, we will therefore focus on ligand field transitions, for which such radical correlation is typically negligible.[47]

For triplet ferryl species, the temperature-dependent behavior of MCD intensity reflects the polarization of a given electronic transition. According to eq 1, the MCD *C*-term intensity is proportional to $\langle S_u \rangle M_{vw}^{\mathrm{eff}}$, where $M_{vw}^{\mathrm{eff}}$ represents the effective transition dipole moment product, and $\langle S_u \rangle$ is the spin expectation value along the *u*-direction (*u*,*v*,*w* = *x*,*y*,*z*). As shown in the VTVH analysis of the MCD spectra (vide supra), complex **1** has a sizable positive axial ZFS parameter *D* of ∼17 cm$^{-1}$ with a small rhombicity parameter *E*/*D* of 0.08. Therefore, the $M_s = 0$ magnetic sublevel lies lower in energy and is separated by ∼17 cm$^{-1}$ (*D*) from the nearly degenerate $M_s = \pm 1$ sublevels. At very low temperatures, only the $M_s = 0$ sublevel needs to be taken in account because the population in the high-energy $M_s = \pm 1$ sublevels is marginal. As such, the spin expectation values are $\langle S_z \rangle = 0$, and $\langle S_x \rangle, \langle S_y \rangle \neq 0$ (Figures S3 and S4), of which the latter two nonvanishing values originate from mixing of different $M_s$ sublevels induced by the applied magnetic field. As a consequence, *z*-polarized transitions acquire MCD intensities. At elevated temperatures, the $M_s = -1$ magnetic sublevel becomes considerably populated; hence, $\langle S_x \rangle, \langle S_y \rangle = 0$ and $\langle S_z \rangle = -1$. Therefore, transitions polarized along *x*,*y*-directions gain MCD intensities. At even higher temperatures, the intensities for all transitions


DOI: 10.1021/jacs.6b07708
J. Am. Chem. Soc. 2016, 138, 14312−14325

drop because the MCD *C*-term intensity is inversely proportional to the temperature (the Curie law). Thus, starting from low temperatures, the intensity for a *z*-polarized transition declines with temperature, while that for a *x,y*-polarized transition first increases and then decreases.

On the basis of the polarization and the computed excitation energy, we can unambiguously assign bands 1 and 2 to E($d_{xy}$ → $d_{xz,yz}$). This process corresponds to an electron transfer from the essentially NB Fe-$d_{xy}$ orbital to the Fe−O $\pi^*$-orbital (Fe-$d_{xz,yz}$), which is expected to cause considerable lengthening of the Fe−O bond. The BP86-optimized geometry of the excited state predicts the Fe−O bond length to be ∼1.78 Å, significantly longer than that (1.66 Å) found in the crystal structure of complex **1**.[19] We have not found other considerable geometric distortions in the computed excited-state geometry relative to that of the ground state. Thus, the fine structure can be attributed to a vibronic Franck−Condon progression mainly in the Fe−O stretching mode. Indeed, the calculated excited-state Fe−O stretching frequency ($\nu_{es}$(Fe−O) = 648 $cm^{-1}$) matches the average spacing of the progression ($\nu_{es}$(Fe−O) = 616 $cm^{-1}$) found experimentally, and the estimated Huang−Rhys factor ($S_{HR}$ = 2.8) is in good agreement with that ($S_{HR}$ = 3.1) determined from the Poisson intensity distribution, thereby lending strong credence to our proposed assignment. The E($d_{xy}$ → $d_{xz,yz}$) electronic transitions for $[Fe^{IV}(O)(TMC)(NCMe)]^{2+}$ and $[Fe^{IV}(O)(N4Py)]^{2+}$ (N4Py = N-(bis(2-pyridyl)-methyl)-N,N-bis(2-pyridylmethyl)-amine) occur in the same energy region (10 600 and 12 600 $cm^{-1}$, respectively) and also exhibit analogous vibronic progressions.[42] The excited-state Fe−O stretching frequency and Huang−Rhys factor measured for complex **1** are similar to those for $[Fe^{IV}(O)(TMC)(NCMe)]^{2+}$ ($\nu_{es}$(Fe−O) = 610 $cm^{-1}$ and $S_{HR}$ = 3), whereas they are considerably different from those found for $[Fe^{IV}(O)(N4Py)]^{2+}$ ($\nu_{es}$(Fe−O) = 500 $cm^{-1}$ and $S_{HR}$ = 4.5).[42] Unsurprisingly, this reflects the structural similarity between complex **1** and $[Fe^{IV}(O)(TMC)(NCMe)]^{2+}$. Unlike bands 4 and 5, another pseudo *A*-term signal, bands 1 and 2 retain nonvanishing intensity even extrapolated to zero Kelvin (Figure 3). Furthermore, our calculations significantly underestimate the transition intensity compared to the experimental spectra, especially at very low temperatures, mainly because the computed intensity does not contain contributions from vibronic coupling. Both observations suggest that the intensity borrowing due to vibronic coupling is likely another noticeable source of the transition probability observed for bands 1 and 2 and that their intrinsic intensity arising from the pure electronic origin may be very low (vide infra).

The temperature-dependent intensity variation indicates that band 3 is a *z*-polarized transition. According to group theory, the excited state must be of $A_2$ symmetry in $C_{4v}$ point group. This points to the two transitions $A_2$($d_{xy}$ → $d_{z2}$) or $A_2$($d_{xy}$ → $d_{x2-y2}$). However, both are two-electron excitations in nature (for details, see the Supporting Information) and hence have negligible transition probabilities. To gain the considerable intensity as shown in Figure 1, they must borrow some intensity from other strongly allowed transitions, for which CT excited states are typically appropriate candidates. Note that in the effective $C_{4v}$ symmetry, there are no other d−d single excitations featuring $A_2$ symmetry (Figure 5). Moreover, lowering the symmetry from $C_{4v}$ to $C_s$, the latter being the actual symmetry of complex **1**, further intensifies mixing of different excited states. This leads to substantial *x,y* fractional polarization factors for band 3 deduced from the VTVH analysis (Table 1). In line with this reasoning, our calculations reveal that both $A_2$ ligand field transitions interact with the LMCT excited states arising from the O-$p_{x,y}$ orbitals to Fe-$d_{xz,yz}$. However, the configuration interaction between ligand field and CT excited states should be underestimated to some extent because our CASSCF/NEVPT2 calculations significantly overestimate the excitation energies for CT transitions, and the energy gaps between ligand field and CT excited states computed at zeroth order are too big. This may explain why the computed excitation energy of the $A_2$ excited state is too high and its intensity is too low because the interaction between two states results in not only intensity borrowing, but also repelling each other with respect to their excitation energies. In addition, the $A_2$ ligand field excited state may interact with other LMCT states involving the supporting ligand. To reach a definite assignment for band 3, CASSCF calculations with prohibitively large active space would be required. Considering the complexities and difficulties to pinpoint this issue, we cannot reach a definitive assignment of band 3 to either $A_2$($d_{xy}$ → $d_{z2}$) or $A_2$($d_{xy}$ → $d_{x2-y2}$). In fact, a similar situation is found for band 6.

We can unambiguously assign bands 4 and 5 to the E($d_{xz,yz}$ → $d_{z2}$) excitations according to their polarization properties and the computed transition energies. To further confirm this assignment, we determine the MCD *C*-term signs for the constituent excitations below. The pseudo *A*-term signal of bands 3 and 4 arises from SOC between the two transitions of $E_x$($d_{xz}$ → $d_{z2}$) and $E_y$($d_{yz}$ → $d_{z2}$) (*J*−*K* coupling). In principal, pure d−d transitions are parity forbidden and hence have vanishing transition probability. The intensity of E($d_{xz,yz}$ → $d_{z2}$) mainly originates from the covalent metal−ligand interaction.[48] Because the metal center moves out of the equatorial plane, the carbene C-p orbitals make substantial contributions to the EDO and the EAO (Figure 7). The E($d_{xz,yz}$ → $d_{z2}$) transitions

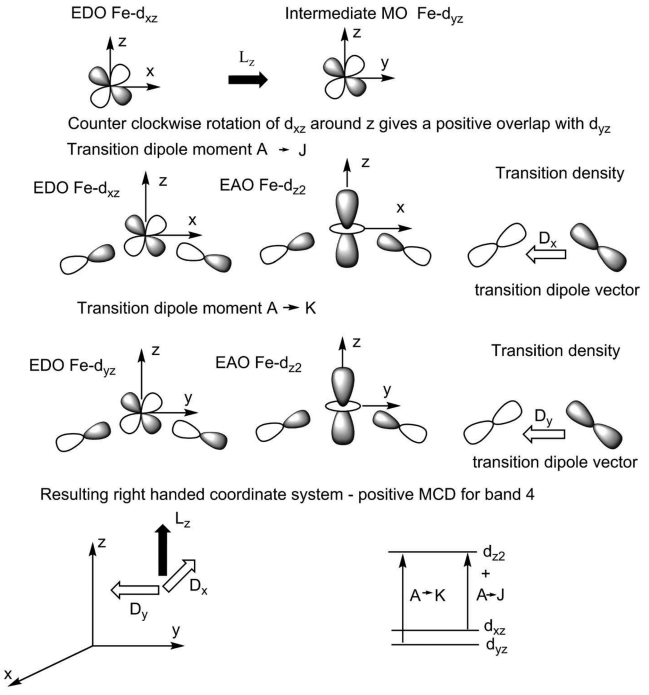


**Figure 7.** Graphical prediction of the *C*-term sign for the $d_{xz}$ → $d_{z2}$ transition. The open and filled orbital contours indicate positive and negative amplitudes.



DOI: 10.1021/jacs.6b07708
J. Am. Chem. Soc. 2016, 138, 14312−14325

are single-electron excitations in nature; therefore, their transition densities and hence transition dipole moments can be easily determined by inspection of the respective EDOs and EAOs.[49] The "overlap" between the fragmental C-p orbitals in the EDO and the EAO leads to considerable transition density, which defines the transition dipole moments of $d_{xz} \rightarrow d_{z2}$ and $d_{yz} \rightarrow d_{z2}$ mainly pointing along $-x$ and $-y$ directions, respectively (Figure 7). Counterclockwise rotation of the $d_{xz}$ orbital into the intermediate $d_{yz}$ orbital around $z$ leads to a positive overlap, and hence, the reduced matrix element of the SOC operator is positive, $\bar{L}_z^{KJ} > 0$. Herein, we assume that the lower energy transition $A \rightarrow J$ is $d_{xz} \rightarrow d_{z2}$, and hence, $A \rightarrow K$ is $d_{yz} \rightarrow d_{z2}$. Note that the specific assignment for a given constituent transition is immaterial for the sign of the entire pseudo $A$-term.[21a] If one assumes $A \rightarrow J$ is $d_{xy} \rightarrow d_{z2}$, and $A \rightarrow K$ is $d_{xz} \rightarrow d_{z2}$, the same results should be obtained. The effective transition dipole moment product for $A \rightarrow J = d_{xz} \rightarrow d_{z2}$ is given by

$$M_{xy}^{\mathrm{eff}}(E_x) \approx \frac{\bar{L}_z^{KJ}}{\Delta_{KJ}}(\vec{D}_x^{AK}\vec{D}_y^{AJ} - \vec{D}_y^{AK}\vec{D}_x^{AJ}) \tag{5}$$

Thus, the MCD $C$-term sign in the saturation limit can be determined as follows:

$$\begin{aligned}\bar{C}_0(E_x) &\propto \langle S_z\rangle \frac{\bar{L}_z^{KJ}}{\Delta_{KJ}}(\vec{D}_x^{AK}\vec{D}_y^{AJ} - \vec{D}_y^{AK}\vec{D}_x^{AJ}) \\ &\propto -|\langle S_z\rangle| \frac{|\bar{L}_z^{KJ}|}{\Delta_{KJ}}(-1)(-|\vec{D}_y^{AK}|)(-|\vec{D}_x^{AJ}|) > 0\end{aligned} \tag{6}$$

with $\Delta_{KJ} = E_K - E_J > 0$.

Alternatively, the sign of this $C$-term transition can be determined in a pictorial way. As shown in Figure 7, the transition dipole moments $D_x$ and $D_y$ for the $A \rightarrow J$ and $A \rightarrow K$ transitions, respectively, and the reduced spin−orbit vector $L_z$ form a right-handed system. It follows that for the positive energy gap $\Delta_{KJ}$ the transition absorbs left-handed photons and thus yields a positive MCD $C$-term. In contrast, the MCD $C$-term signal of the higher-energy $d_{yz} \rightarrow d_{z2}$ transition has a negative sign. Note that in the present situation $A \rightarrow J = d_{yz} \rightarrow d_{z2}$, and $A \rightarrow K = d_{xz} \rightarrow d_{z2}$, one need therefore rotate the $d_{yz}$ orbital into the intermediate $d_{xz}$ orbital:

$$\begin{aligned}\bar{C}_0(E_y) &\propto \langle S_z\rangle \frac{\bar{L}_z^{KJ}}{\Delta_{KJ}}(\vec{D}_x^{AK}\vec{D}_y^{AJ} - \vec{D}_y^{AK}\vec{D}_x^{AJ}) \\ &\propto -|\langle S_z\rangle| \frac{-|\bar{L}_z^{KJ}|}{\Delta_{KJ}}(-|\vec{D}_x^{AK}|)(-|\vec{D}_y^{AJ}|) < 0\end{aligned} \tag{7}$$

with $\Delta_{KJ} = E_K - E_J < 0$.

Taken together, the transitions $E(d_{xz} \rightarrow d_{z2})$ and $E(d_{yz} \rightarrow d_{z2})$ give rise to a negative pseudo $A$-term signal. The same transitions have also been observed in the MCD spectra of high spin ferryl complex $[Fe^{IV}(O)(TMG_3tren)]^{2+}$ ($TMG_3tren$ =1,1,1-tris{2-[$N^2$-(1,1,3,3-tetramethylguanidino)]ethyl}amine) and the ferryl intermediate in halogenase SyrB2, and the sign of the corresponding pseudo $A$-term signals is negative, too.[22d,g]

Similarly, we can reach an unequivocal assignment for bands 7 and 8 to $E(d_{xz,yz} \rightarrow d_{x2\text{-}y2})$ by determining its pseudo $A$-term sign (Figure S5). Unlike the $d_{z2}$-centered EAO having the same phase in the equatorial plane, the phase of the C-p contributions in the $d_{x2\text{-}y2}$-based EAO have opposite sign along the $x$-direction relative to that along the $y$-direction. Therefore, relative to the transitions to the $d_{z2}$ orbital, one of the transition dipole moments for $d_{xz} \rightarrow d_{x2\text{-}y2}$ and $d_{yz} \rightarrow d_{x2\text{-}y2}$ changes to the opposite direction, but the other is unaffected. This reverses the MCD $C$-term sign for the individual transition from the same EDO and hence the sign of the entire pseudo $A$-term. The same transitions found for complex **2**[40] and related ferryl complexes[42] displays a positive pseudo $A$-term signal as well.

As elaborated above, the high absorption intensities measured for bands 4, 5, 7, and 8 originate mainly from covalency effects,[48] while for bands 1 and 2, because their EDOs are essentially NB orbitals with marginal contributions from the supporting ligand, their transition probability is much lower as observed in the absorption spectrum in Figure 1.

In summary, an unambiguous assignment can be reached for the three pseudo $A$-term transitions. As shown in Table 2, for the four excitations starting from the same EDOs, $d_{xz,yz}$, the $d_{xz,yz} \rightarrow d_{z2}$ transitions found for compound **1** (bands 4, 5) exhibit much lower excitation energies than the $d_{xz,yz} \rightarrow d_{x2\text{-}y2}$ transitions (bands 7,8). In contrast, for complex **2**[40] and the related ferryl complexes,[42] the order is opposite. This verifies the notion that the ground-state electron configuration of complex **1** is best formulated as $\sigma(\text{O-p}_z)^2\pi(\text{O-p}_{x,y})^4\text{NB}(\text{Fe-d}_{xy})^2\pi^*(\text{Fe-d}_{xz,yz})^2\sigma^*(\text{Fe-d}_{z2})^0\sigma^*(\text{Fe-d}_{x2\text{-}y2})^0$, in which the Fe-$d_{z2}$ orbital is situated lower in energy than Fe-$d_{x2\text{-}y2}$ (Scheme 1c). Note that such information cannot be obtained by direct comparison of the excitation energies for the two $A_2$ excited states because they involve complex multiplet effects and spin coupling pattern. To the best of our knowledge, this unusual electronic structure has not been proven experimentally before, although it has been postulated for related ferryl complexes containing strong equatorial $\sigma$-donating ligands.[9,10] Relative to other well characterized triplet ferryl complexes, such as complex **2**[40] and $[Fe^{IV}(O)(TMC)(NCMe)]^{2+}$,[42] similar excitation energies were found for the transitions within the $(FeO)^{2+}$ core ($d_{xy} \rightarrow d_{xz,yz}$ and $d_{xz,yz} \rightarrow d_{z2}$). Furthermore, we can determine the ground state Fe−O stretch of complex **1** occurring at 832 ± 3 $cm^{-1}$ and the same vibration in the $E(d_{xy} \rightarrow d_{xz,yz})$ excited state at 616 ± 15 $cm^{-1}$, both values analogous to those reported for $[Fe^{IV}(O)(TMC)(NCMe)]^{2+}$.[42] Therefore, all the experimental findings indicate that the change of the equatorial ligand from polydentate N donors to tetracarbene does not discernibly perturb the bonding in the $Fe^{IV}$-oxo unit and that the strong supporting ligand only pushes up the $d_{x2-y2}$ orbital such that it is situated higher in energy than the $d_{z2}$ orbital. This experimentally validated electronic structure leads to decisive mechanistic consequences for the HAT processes with complex **1**.

**3.6. Ligand Field Analysis of the Ab Initio and Experimental Results.** The distinct electronic structures of **1** and **2** can be attributed to the chemical donor capabilities of the supporting ligands by invoking AILFT analyses of orbital- and state-ordering, which yield the 3d orbital diagrams shown in Figure S7. In contrast to the rather heuristic correlation of many-particle states to dominating one-electron orbital contributions applied so far, the AILFT orbital energies deduced from the ab initio calculations reflect the chemical metal−ligand interactions but do not include electron correlations or Coulomb repulsion (parametrized by the Racah parameter $B$). Therefore, the AILFT orbital picture shows a strong destabilization of the $d_{x2\text{-}y2}$ orbital by more than 10 000 $cm^{-1}$ for complex **1** with respect to complex **2** due to the strong in-plane $\sigma$-interaction of the tetracarbene ligand, but


DOI: 10.1021/jacs.6b07708
J. Am. Chem. Soc. 2016, 138, 14312−14325

Table 2. Comparison of Excitation Energies ($cm^{-1}$) of Key d–d Transitions

| | complex 1[a] | | complex 2[b] | | [Fe(O)(TMC)(NCMe)]$^{2+c}$ | [Fe(O)(TMC)(OC(O)$CF_3$)]$^{+c}$ | [Fe(O)(N4Py)]$^{2+c}$ |
|---|---|---|---|---|---|---|---|
| transition | exp. | calc. | exp. | calc. | exp. | exp. | exp. |
| $^3E(1b_2 \rightarrow 2e)$ $d_{xy} \rightarrow d_{xz,yz}$ | 12 410, 12 930 | 13 100, 13 200 | | 13 320, 13 400 | 10 060 | 11 100 | 12 600 |
| $^3E(2e \rightarrow 2a_1)$ $d_{xz,yz} \rightarrow d_{z2}$ | 15 700, 18 220 | 18 820, 18 860 | 18 200 | 17 960, 18 050 | 17 600 | | |
| $^3E(2e \rightarrow 2b_1)$ $d_{xz,yz} \rightarrow d_{x2-y2}$ | 22 660, 25 920 | 25 010, 25 160 | 13 700, 15 220 | 11 840, 12 060 | 12 900 | 12 000 | 15 100 |

[a]Values taken from Table 1. [b]The values are quoted from ref 40. The $^3E(1b_2 \rightarrow 2e)$ transition and the other component for $^3E(2e \rightarrow 2a_1)$ have not been well resolved experimentally because they superimpose with other intense transitions. [c]The values are quoted from ref 42.

not yet a crossover with $d_{z2}$. In AILFT terms, the difference of carbene and pyridine ligands is manifested by significantly different angular overlap model (AOM) parameters $e_\sigma$ of about 9800 $cm^{-1}$ found for complex **1** and about 7400 $cm^{-1}$ for complex **2**. This raises the energy of the $d_{x2-y2}$ orbital in complex **1** by about 7200 $cm^{-1}$, three-times the difference $\Delta e_\sigma$.

The experimentally established crossover of state energies is finally afforded by a large difference of 14*B*, calculated in the AILFT formalism for the repulsion of electrons in $d_{x2-y2}$ and $d_{z2}$ orbitals (eqs S4 and S5). The full AILFT analysis for both compounds and the resulting AOM parameters are given in the Supporting Information.

**3.7. Mechanistic Implications.** For usual synthetic triplet ferryl species supported by polydentate N-donor ligands, the lowest-energy quintet excited state features an electron configuration of $\sigma(O\text{-}p_z)^2\pi(O\text{-}p_{x,y})^4NB(Fe\text{-}d_{xy})^1\pi^*(Fe\text{-}d_{xz,yz})^2\sigma^*(Fe\text{-}d_{x2-y2})^1\sigma^*(Fe\text{-}d_{z2})^0$ (Scheme 1b), which can be regarded as a spin-flip excited state from the NB $d_{xy}$ orbital to the $\sigma^*_{eq}$ $d_{x2-y2}$ orbital. As expected, the Fe–O bond distances are nearly identical for both states, whereas the metal–ligand bonds in the equatorial plane slightly lengthen in the spin-flip transition. The weaker supporting N-donor ligands, in contrast to the macrocyclic tetracarbene ligand of complex **1**, can easily accommodate this geometry distortion; hence, both states are close in energy with the quintet state lying ~3 kcal/mol above the triplet state.[5] The computed Fe–O bond distance (1.73 Å) for the quintet excited state of complex **1** is significantly longer than that (1.66 Å) found for its triplet ground state,[19] consistent with an electron configuration of $\sigma(O\text{-}p_z)^2\pi(O\text{-}p_{x,y})^4NB(Fe\text{-}d_{xy})^1\pi^*(Fe\text{-}d_{xz,yz})^2\sigma^*(Fe\text{-}d_{z2})^1\sigma^*(Fe\text{-}d_{x2-y2})^0$, in which one electron is occupied in the Fe–O $\sigma^*$-orbital ($d_{z2}$). The substantial Fe–O bond lengthening between the triplet ground state and the quintet state, a significant geometric rearrangement, rationalizes the larger triplet-quintet energy gap calculated by DFT (18.7 kcal/mol). An even larger energy splitting (28.3 kcal/mol) is delivered by our state-specific CASSCF/NEVPT2 calculations, indicating that the DFT computations may underestimate this energy separation because DFT approaches often fail in predicting accurate spin-state energetics.[50] For $[Fe^{IV}(O)(NH_3)_5]^{2+}$, the barrier for the most efficient HAT pathway on the triplet surface is computed to be 16.3 kcal/mol by DFT.[12d] Both observations clearly suggest that the HAT process mediated by complex **1** is unlikely to proceed on the quintet surface. In HAT, only the Fe-$d_{xz,yz}$ and $-d_{z2}$ orbitals function as the EAOs, whereas the Fe-$d_{xy}$ and $-d_{x2-y2}$ orbitals only can act as spectators.[12d,f,g,j] Therefore, the reactivity of complex **1** should represent the pure, intrinsic reactivity of a ferryl species in the triplet state without the complications due to the quintet state because its Fe–O bonding is nearly identical to that found for usual ferryl compounds with N-donor supporting ligands. Hence, this system may enable us for the first time to obtain the intrinsic efficacy of a triplet ferryl species toward HAT, as opposed to earlier reactivity studies that are subjected to the ambiguities arising from possible two-state reactivity, a major step forward toward a better understanding of the reaction mechanism of C–H bond activation carried out by high-valent oxo–iron(IV) species. An experimental reactivity study following this line is in progress.

## 4. CONCLUSION

In this work, a detailed analysis of the electronic structure of a tetracarbene oxo–iron(IV) species (complex **1**) using a



DOI: 10.1021/jacs.6b07708
J. Am. Chem. Soc. 2016, 138, 14312–14325

combined experimental and theoretical approach is presented. We are able to unambiguously assign the important ligand field transitions through direct computations of MCD spectra with wave function based multireference method and independent determination of the MCD *C*-term signs. In contrast to the majority of triplet ferryl complexes supported by polydentate N-donor ligands, complex **1** has been proven to feature a distinct electron configuration in which the $d_{x2-y2}$ orbital lies higher in energy than $d_{z2}$. Our detailed electronic-structure analysis by using MCD and IRPD spectroscopy clearly show that the tetracarbene ligand of complex **1** does not considerably affect the bonding in the $(FeO)^{2+}$ core but strongly destabilizes the $d_{x2-y2}$ orbital and lifts it above the $d_{z2}$ orbital in energy. As a result, the HAT reaction with complex **1** is likely to exclusively take place on the triplet surface due to the large quintet−triplet energy gap. The resulting mechanistic implications are also discussed.

## ■ ASSOCIATED CONTENT

### Supporting Information

The Supporting Information is available free of charge on the ACS Publications website at DOI: 10.1021/jacs.6b07708.

Details on experimental analysis; CASSCF/NEVPT2 calculations and ligand field analysis; Cartesian coordinates of all optimized structures (PDF)

## ■ AUTHOR INFORMATION


### Corresponding Authors

*shengfa.ye@cec.mpg.de
*mihail.atanasov@cec.mpg.de
*ebill@gwdg.de
*jana.roithova@natur.cuni.cz
*franc.meyer@chemie.uni-goettingen.de
*frank.neese@cec.mpg.de


### Notes

The authors declare no competing financial interest.

## ■ ACKNOWLEDGMENTS

We are indebted to Andreas Göbels for MCD measurements and Prof. Larry Que (University of Minnesota) for fruitful discussions. S.Y., O.K., B.M., M.A., E.B., and F.N. gratefully acknowledge financial support from the Max-Planck Society. C.K., S.M., and F.M. gratefully acknowledge support by the Fonds der Chemischen Industrie (Kekulé scholarship for C.K.) and the DFG (IRTG 1422 "Metal Sites in Biomolecules: Structures, Regulation and Mechanisms"). E.A., R.N., and J.R. thank the Grant Agency of the Czech Republic (14-20077S) for the financial support. This work has been performed in the framework of the European COST program CM 1305 (with support of an STSM of C.K. to Prague).

## ■ REFERENCES


(1) (a) Solomon, E. I.; Brunold, T. C.; Davis, M. I.; Kemsley, J. N.; Lee, S.-K.; Lehnert, N.; Neese, F.; Skulan, A. J.; Yang, Y.-S.; Zhou, J. *Chem. Rev.* **2000**, *100*, 235−349. (b) Costas, M.; Mehn, M. P.; Jensen, M. P.; Que, L., Jr. *Chem. Rev.* **2004**, *104*, 939−986. (c) Groves, J. T. *J. Inorg. Biochem.* **2006**, *100*, 434−447.

(2) *Cytochrome P450: Structure, Mechanism and Biochemistry*, 3rd ed.; Ortiz de Montellano, P. R., Ed.; Kluwer Academic/Plenum Publisher: New York, 2004.

(3) (a) Green, M. T.; Dawson, J. H.; Gray, H. B. *Science* **2004**, *304*, 1653−1656. (b) Green, M. T. *Curr. Opin. Chem. Biol.* **2009**, *13*, 84−88. (c) Schulz, C. E.; Rutter, R.; Sage, J. T.; Debrunner, P. G.; Hager, L. P. *Biochemistry* **1984**, *23*, 4743−4654. (d) Rutter, R.; Hager, L. P.; Dhonau, H.; Hendrich, M.; Valentine, M.; Debrunner, P. *Biochemistry* **1984**, *23*, 6809−6816. (e) Debrunner, P. G. Iron Porphyrins Part III. *Physical Bioinorganic Chemistry*; Lever, A. B. P., Gray, H. B., Eds.; Wiley-VCH: Weinheim, 1989; Vol. *III*, p 137.

(4) (a) Krebs, C.; Galonić Fujimori, D.; Walsh, C. T.; Bollinger, J. M., Jr. *Acc. Chem. Res.* **2007**, *40*, 484−492. (b) Hausinger, R. P. *Crit. Rev. Biochem. Mol. Biol.* **2004**, *39*, 21−68. (c) Fitzpatrick, P. F. *Biochemistry* **2003**, *42*, 14083−14091.

(5) Ye, S.; Geng, C.-Y.; Shaik, S.; Neese, F. *Phys. Chem. Chem. Phys.* **2013**, *15*, 8017−8030. (b) Neese, F. *J. Inorg. Biochem.* **2006**, *100*, 716−726. (c) Sinnecker, S.; Svensen, N.; Barr, E. W.; Ye, S.; Bollinger, J. M., Jr.; Neese, F.; Krebs, C. *J. Am. Chem. Soc.* **2007**, *129*, 6168−6179.

(6) (a) Que, L., Jr. *Acc. Chem. Res.* **2007**, *40*, 493−500. (b) Nam, W. *Acc. Chem. Res.* **2007**, *40*, 522−531. (c) McDonald, A. R.; Que, L., Jr. *Coord. Chem. Rev.* **2013**, *257*, 414−428.

(7) Pestovsky, O.; Stoian, S.; Bominaar, E. L.; Shan, X.; Münck, E.; Que, L., Jr.; Bakac, A. *Angew. Chem., Int. Ed.* **2005**, *44*, 6871−6874.

(8) (a) Biswas, A. N.; Puri, M.; Meier, K. K.; Oloo, W. N.; Rohde, G. T.; Bominaar, E. L.; Münck, E.; Que, L., Jr. *J. Am. Chem. Soc.* **2015**, *137*, 2428−2431. (b) Puri, M.; Biswas, A. N.; Fan, R.; Guo, Y.; Que, L. *J. Am. Chem. Soc.* **2016**, *138*, 2484−2487.

(9) Chanda, A.; Shan, X.; Chakrabarti, M.; Ellis, W. C.; Popescu, D. L.; Tiago de Oliveira, F.; Wang, D.; Que, L., Jr.; Collins, T. J.; Münck, E.; Bominaar, E. L. *Inorg. Chem.* **2008**, *47*, 3669−3678.

(10) (a) Shaik, S.; Kumar, D.; de Visser, S. P.; Altun, A.; Thiel, W. *Chem. Rev.* **2005**, *105*, 2279−2328. (b) Shaik, S.; Cohen, S.; Wang, Y.; Chen, H.; Kumar, D.; Thiel, W. *Chem. Rev.* **2010**, *110*, 949−1017.

(11) (a) England, J.; Guo, Y.; Van Heuvelen, K. M.; Cranswick, M. A.; Rohde, G. T.; Bominaar, E. L.; Münck, E.; Que, L., Jr. *J. Am. Chem. Soc.* **2011**, *133*, 11880−11883. (b) England, J.; Guo, Y.; Farquhar, E. R.; Young, V. G., Jr.; Münck, E.; Que, L., Jr. *J. Am. Chem. Soc.* **2010**, *132*, 8635−8644. (c) England, J.; Martinho, M.; Farquhar, E. R.; Frisch, J. R.; Bominaar, E. L.; Münck, E.; Que, L., Jr. *Angew. Chem., Int. Ed.* **2009**, *48*, 3622−3626. (d) Bigi, J. P.; Harman, W. H.; Lassalle-Kaiser, B.; Robles, D. M.; Stich, T. A.; Yano, J.; Britt, R. D.; Chang, C. J. *J. Am. Chem. Soc.* **2012**, *134*, 1536−1542. (e) Lacy, D. C.; Gupta, R.; Stone, K. L.; Greaves, J.; Ziller, J. W.; Hendrich, M. P.; Borovik, A. S. *J. Am. Chem. Soc.* **2010**, *132*, 12188−12190.

(12) (a) Johansson, A. J.; Blomberg, M. R. A.; Siegbahn, P. E. M. *J. Phys. Chem. C* **2007**, *111*, 12397−12406. (b) Bernasconi, L.; Baerends, E. I. *Eur. J. Inorg. Chem.* **2008**, *2008*, 1672−1681. (c) Ye, S.; Neese, F. *Curr. Opin. Chem. Biol.* **2009**, *13*, 89−98. (d) Geng, C.-Y.; Ye, S.; Neese, F. *Angew. Chem., Int. Ed.* **2010**, *49*, 5717−5720. (e) Shaik, S.; Chen, H.; Janardanan, D. *Nat. Chem.* **2011**, *3*, 19−27. (f) Ye, S.; Neese, F. *Proc. Natl. Acad. Sci. U. S. A.* **2011**, *108*, 1228−1233. (g) Janardanan, D.; Usharani, D.; Chen, H.; Shaik, S. *J. Phys. Chem. Lett.* **2011**, *2*, 2610−2617. (h) Verma, P.; Vogiatzis, K. D.; Planas, N.; Borycz, J.; Xiao, D. J.; Long, J. R.; Gagliardi, L.; Truhlar, D. G. *J. Am. Chem. Soc.* **2015**, *137*, 5770−5781. (i) Andris, E.; Jašík, J.; Gomez, L.; Costas, M.; Roithová, J. *Angew. Chem., Int. Ed.* **2016**, *55*, 3637−3641. (j) Mondal, B.; Roy, L.; Neese, F.; Ye, S. *Isr. J. Chem.* **2016**, *56*, 763−772.

(13) Xue, G.; De Hont, R.; Münck, E.; Que, L., Jr. *Nat. Chem.* **2010**, *2*, 400−405.

(14) (a) Sastri, C. V.; Lee, J. J.; Oh, K.; Lee, Y. J.; Jackson, T. A.; Ray, K.; Hirao, H.; Shin, W.; Halfen, J. A.; Kim, J.; Que, L., Jr.; Shaik, S.; Nam, W.; Lee, J. *Proc. Natl. Acad. Sci. U. S. A.* **2007**, *104*, 19181−19186. (b) Hirao, H.; Kumar, D.; Que, L., Jr.; Shaik, S. *J. Am. Chem. Soc.* **2006**, *128*, 8590−8606. (c) Hirao, H.; Que, L.; Nam, W.; Shaik, S. *Chem. - Eur. J.* **2008**, *14*, 1740−1756.

(15) (a) Mandal, D.; Shaik, S. *J. Am. Chem. Soc.* **2016**, *138*, 2094−2097. (b) Kwon, Y. H.; Mai, B. K.; Lee, Y.-M.; Dhuri, S. N.; Mandal, D.; Cho, K.-B.; Kim, Y.; Shaik, S.; Nam, W. *J. Phys. Chem. Lett.* **2015**, *6*, 1472−1476.

(16) Cho, K.-B.; Wu, X.; Lee, Y.-M.; Kwon, Y. H.; Shaik, S.; Nam, W. *J. Am. Chem. Soc.* **2012**, *134*, 20222−20225.

(17) Hong, S.; So, H.; Yoon, H.; Cho, K.-B.; Lee, Y.-M.; Fukuzumi, S.; Nam, W. *Dalton Trans.* **2013**, *42*, 7842−7845.

(18) Lim, M. H.; Rohde, J.-U.; Stubna, A.; Bukowski, M. R.; Costas, M.; Ho, R. Y. N.; Münck, E.; Nam, W.; Que, L. *Proc. Natl. Acad. Sci. U. S. A.* **2003**, *100*, 3665−3670.
(19) Meyer, S.; Klawitter, I.; Demeshko, S.; Bill, E.; Meyer, F. *Angew. Chem., Int. Ed.* **2013**, *52*, 901−905.
(20) For selected examples: (a) Solomon, E. I.; Lever, A. B. P. *Inorganic Electronic Structure and Spectroscopy*; Wiley Interscience: Hoboken, NJ, 2006; Vol. *I*. (b) Farrar, J. A.; Neese, F.; Lappalainen, P.; Kroneck, P. M. H.; Saraste, M.; Zumft, W. G.; Thomson, A. J. *J. Am. Chem. Soc.* **1996**, *118*, 11501−11514. (d) Neese, F.; Solomon, E. I. *J. Am. Chem. Soc.* **1998**, *120*, 12829−12848. (e) Gamelin, D. R.; Randall, D. W.; Hay, M. T.; Houser, R. P.; Mulder, T. C.; Canters, G. W.; de Vries, S.; Tolman, W. B.; Lu, Y.; Solomon, E. I. *J. Am. Chem. Soc.* **1998**, *120*, 5246−5263. (f) Paulat, F.; Lehnert, N. *Inorg. Chem.* **2008**, *47*, 4963−4976. (g) Johansson, F. B.; Bond, A. D.; Nielsen, U. G.; Moubaraki, B.; Murray, K. S.; Berry, K. J.; Larrabee, J. A.; McKenzie, C. J. *Inorg. Chem.* **2008**, *47*, 5079−5092. (h) Larrabee, J. A.; Johnson, W. R.; Volwiler, A. S. *Inorg. Chem.* **2009**, *48*, 8822−8829. (i) Gamelin, D. R.; Kirk, M. L.; Stemmler, T. L.; Pal, S.; Armstrong, W. H.; Pennerhahn, J. E.; Solomon, E. I. *J. Am. Chem. Soc.* **1994**, *116*, 2392−2399. (j) Brunold, T. C.; Gamelin, D. R.; Stemmler, T. L.; Mandal, S. K.; Armstrong, W. H.; Penner-Hahn, J. E.; Solomon, E. I. *J. Am. Chem. Soc.* **1998**, *120*, 8724−8738. (k) Brunold, T. C.; Gamelin, D. R.; Solomon, E. I. *J. Am. Chem. Soc.* **2000**, *122*, 8511−8523. (l) Jackson, T. A.; Karapetian, A.; Miller, A. F.; Brunold, T. C. *J. Am. Chem. Soc.* **2004**, *126*, 12477−12491. (m) Geiger, R. A.; Chattopadhyay, S.; Day, V. W.; Jackson, T. A. *J. Am. Chem. Soc.* **2010**, *132*, 2821−2831. (n) Chattopadhyay, S.; Geiger, R. A.; Yin, G. C.; Busch, D. H.; Jackson, T. A. *Inorg. Chem.* **2010**, *49*, 7530−7535. (o) Bane, K.; Geiger, R. A.; Chabolla, S. A.; Jackson, T. A. *Inorg. Chim. Acta* **2012**, *380*, 135−140. (p) Whittaker, J. W.; Whittaker, M. M. *J. Am. Chem. Soc.* **1991**, *113*, 5528−5540. (q) Mack, J.; Stillman, M. J.; Kobayashi, N. *Coord. Chem. Rev.* **2007**, *251*, 429−453. (r) Lehnert, N. *J. Inorg. Biochem.* **2012**, *110*, 83−93.
(21) (a) Neese, F.; Solomon, E. I. *Inorg. Chem.* **1999**, *38*, 1847−1865. (b) Oganesyan, V. S.; George, S. J.; Cheesman, M. R.; Thomson, A. J. *J. Chem. Phys.* **1999**, *110*, 762−777. (c) Oganesyan, V. S.; Thomson, A. J. *J. Chem. Phys.* **2000**, *113*, 5003−5017. (d) McInnes, E. J. L.; Pidcock, E.; Oganesyan, V. S.; Cheesman, M. R.; Powell, A. K.; Thomson, A. J. *J. Am. Chem. Soc.* **2002**, *124*, 9219−9228. (e) Cheesman, M. R.; Oganesyan, V. S.; Watmough, N. J.; Butler, C. S.; Thomson, A. J. *J. Am. Chem. Soc.* **2004**, *126*, 4157−4166. (f) Oganesyan, V. S.; Cheesman, M. R.; Thomson, A. J. *Inorg. Chem.* **2007**, *46*, 10950−10952.
(22) (a) Westphal, A.; Broda, H.; Kurz, P.; Neese, F.; Tuczek, F. *Inorg. Chem.* **2012**, *51*, 5748−5763. (b) Westphal, A.; Klinkebiel, A.; Berends, H.-M.; Broda, H.; Kurz, P.; Tuczek, F. *Inorg. Chem.* **2013**, *52*, 2372−2387. (c) Woertink, J. S.; Tian, L.; Maiti, D.; Lucas, H. R.; Himes, R. A.; Karlin, K. D.; Neese, F.; Würtele, C.; Holthausen, M. C.; Bill, E.; Sundermeyer, J.; Schindler, S.; Solomon, E. I. *Inorg. Chem.* **2010**, *49*, 9450−9459. (d) Srnec, M.; Wong, S. D.; England, J.; Que, L., Jr.; Solomon, E. I. *Proc. Natl. Acad. Sci. U. S. A.* **2012**, *109*, 14326−14331. (e) Carducci, M. D.; Brown, C.; Solomon, E. I.; Enemark, J. H. *J. Am. Chem. Soc.* **1994**, *116*, 11856−11868. (f) Gewirth, A. A.; Solomon, E. I. *J. Am. Chem. Soc.* **1988**, *110*, 3811−3819. (g) Srnec, M.; Wong, S. D.; Matthews, M. L.; Krebs, C.; Bollinger, J. M.; Solomon, E. I. *J. Am. Chem. Soc.* **2016**, *138*, 5110−5122.
(23) (a) Kapre, R.; Ray, K.; Sylvestre, I.; Weyhermüller, T.; DeBeer-George, S.; Neese, F.; Wieghardt, K. *Inorg. Chem.* **2006**, *45*, 3499−3509. (b) Ray, K.; Begum, A.; Weyhermüller, T.; Piligkos, S.; van Slageren, J.; Neese, F.; Wieghardt, K. *J. Am. Chem. Soc.* **2005**, *127*, 4403−4415. (c) Bill, E.; Bothe, E.; Chaudhuri, P.; Chlopek, K.; Herebian, D.; Kokatam, S.; Ray, K.; Weyhermüller, T.; Neese, F.; Wieghardt, K. *Chem. - Eur. J.* **2005**, *11*, 204−224. (d) Paine, T.; Bothe, E.; Bill, E.; Weyhermüller, T.; Slep, L. D.; Neese, F.; Chaudhuri, P.; Wieghardt, K. *Inorg. Chem.* **2004**, *43*, 7324−7338. (e) Lehnert, N.; Neese, F.; Ho, R. Y. N.; Que, L., Jr.; Solomon, E. I. *J. Am. Chem. Soc.* **2002**, *124*, 10810−10822. (f) Davis, M. I.; Orville, A. M.; Neese, F.; Zaleski, J. M.; Lipscomb, J. D.; Solomon, E. I. *J. Am. Chem. Soc.* **2002**, *124*, 602−614. (g) Neese, F.; Zaleski, J. M.; Loeb Zaleski, K.; Solomon, E. I. *J. Am. Chem. Soc.* **2000**, *122*, 11703−11724.
(24) (a) Piligkos, S.; Slep, L. D.; Weyhermüller, T.; Chaudhuri, P.; Bill, E.; Neese, F. *Coord. Chem. Rev.* **2009**, *253*, 2352−2362. (b) Mitić, N.; Clay, M. D.; Saleh, L.; Bollinger, J. M.; Solomon, E. I. *J. Am. Chem. Soc.* **2007**, *129*, 9049−9065. (c) Kwak, Y.; Jiang, W.; Dassama, L. M. K.; Park, K.; Bell, C. B., III; Liu, L. V.; Wong, S. D.; Saito, M.; Kobayashi, Y.; Kitao, S.; Seto, M.; Yoda, Y.; Alp, E. E.; Zhao, J.; Bollinger, M., Jr.; Krebs, C.; Solomon, E. I. *J. Am. Chem. Soc.* **2013**, *135*, 17573−17584.
(25) (a) Sutherland, J. C.; Holmquist, B. *Annu. Rev. Biophys. Bioeng.* **1980**, *9*, 293−326. (b) Stephens, P. J. *Annu. Rev. Phys. Chem.* **1974**, *25*, 201−232. (c) Stephens, P. J. *Adv. Chem. Phys.* **1976**, *35*, 197−264. (d) Dooley, D. M.; Dawson, J. H. *Coord. Chem. Rev.* **1984**, *60*, 1−66. (e) Solomon, E. I.; Pavel, E. G.; Loeb, K. E.; Campochiaro, C. *Coord. Chem. Rev.* **1995**, *144*, 369−460.
(26) (a) Hernandez-Marin, E.; Seth, M.; Ziegler, T. *Inorg. Chem.* **2010**, *49*, 1566−1576. (b) Seth, M.; Ziegler, T.; Autschbach, J. *J. Chem. Phys.* **2008**, *129*, 104105. (c) Seth, M.; Ziegler, T. *Adv. Inorg. Chem.* **2010**, *62*, 41−109. (d) Seth, M.; Ziegler, T.; Autschbach, J. *J. Chem. Theory Comput.* **2007**, *3*, 434−447. (e) Seth, M.; Ziegler, T. *Chem. Phys.* **2012**, *395*, 63−74.
(27) Bolvin, H. *Inorg. Chem.* **2007**, *46*, 417−427.
(28) Roos, B. O. *Adv. Chem. Phys.* **1987**, *69*, 399−455.
(29) (a) Angeli, C.; Cimiraglia, R.; Evangelisti, S.; Leininger, T.; Malrieu, J. P. *J. Chem. Phys.* **2001**, *114*, 10252−10264. (b) Angeli, C.; Cimiraglia, R.; Malrieu, J. P. *J. Chem. Phys.* **2002**, *117*, 9138−9153.
(30) (a) Ganyushin, D.; Neese, F. *J. Chem. Phys.* **2008**, *128*, 114117. (b) Sundararajan, M.; Ganyushin, D.; Ye, S.; Neese, F. *Dalton Trans.* **2009**, 6021−6036.
(31) (a) Jašík, J.; Žabka, J.; Roithová, J.; Gerlich, D. *Int. J. Mass Spectrom.* **2013**, *354*−*355*, 204−210. (b) Jašík, J.; Gerlich, D.; Roithová, J. *J. Phys. Chem. A* **2015**, *119*, 2532−2542.
(32) Neese, F. *WIREs Comput. Mol. Sci.* **2012**, *2*, 73−78.
(33) (a) Becke, A. D. *Phys. Rev. A: At., Mol., Opt. Phys.* **1988**, *38*, 3098−3100. (b) Perdew, J. P. *Phys. Rev. B: Condens. Matter Mater. Phys.* **1986**, *34*, 7406. (c) Perdew, J. P. *Phys. Rev. B: Condens. Matter Mater. Phys.* **1986**, *33*, 8822−8824.
(34) Grimme, S. *J. Comput. Chem.* **2006**, *27*, 1787−1799.
(35) Schäfer, A.; Huber, C.; Ahlrichs, R. *J. Chem. Phys.* **1994**, *100*, 5829−5835.
(36) (a) Neese, F.; Wennmohs, F.; Hansen, A.; Becker, U. *Chem. Phys.* **2009**, *356*, 98−109. (b) Kossmann, S.; Neese, F. *Chem. Phys. Lett.* **2009**, *481*, 240−243. (c) Izsák, R.; Neese, F.; Klopper, W. *J. Chem. Phys.* **2013**, *139*, 094111. (d) Izsák, R.; Neese, F. *J. Chem. Phys.* **2011**, *135*, 144105.
(37) (a) Eichkorn, K.; Treutler, O.; Ohm, H.; Häser, M.; Ahlrichs, R. *Chem. Phys. Lett.* **1995**, *242*, 652−660. (b) Eichkorn, K.; Weigend, F.; Treutler, O.; Ahlrichs, R. *Theor. Chem. Acc.* **1997**, *97*, 119−124.
(38) Klamt, A.; Schüürmann, G. *J. Chem. Soc., Perkin Trans. 2* **1993**, *2*, 799−805.
(39) Petrenko, T.; Neese, F. *J. Chem. Phys.* **2012**, *137*, 234107.
(40) Ye, S.; Xue, G.; Krivokapic, I.; Petrenko, T.; Bill, E.; Que, L., Jr.; Neese, F. *Chem. Sci.* **2015**, *6*, 2909−2921.
(41) (a) Atanasov, M.; Ganyushin, D.; Sivalingam, K.; Neese, F. Molecular Electronic Structures of Transition Metal Complexes II. *Struct. Bonding (Berlin)*; Mingos, D. M. P., Day, P., Dahl, J. P., Eds.; Springer: Berlin Heidelberg, 2012; pp 149−220. (b) Schweinfurth, D.; Sommer, M. G.; Atanasov, M.; Demeshko, S.; Hohloch, S.; Meyer, F.; Neese, F.; Sarkar, B. *J. Am. Chem. Soc.* **2015**, *137*, 1993−2005.
(42) (a) Decker, A.; Rohde, J.-U.; Que, L., Jr.; Solomon, E. I. *J. Am. Chem. Soc.* **2004**, *126*, 5378−5379. (b) Decker, A.; Rohde, J.-U.; Klinker, E. J.; Wong, S. D.; Que, L., Jr.; Solomon, E. I. *J. Am. Chem. Soc.* **2007**, *129*, 15983−15996.
(43) Roithová, J.; Gray, A.; Andris, E.; Jašík, J.; Gerlich, D. *Acc. Chem. Res.* **2016**, *49*, 223−230.
(44) Jackson, T. A.; Rohde, J.-U.; Seo, M. S.; Sastri, C. V.; DeHont, R.; Ohta, T.; Kitagawa, T.; Münck, E.; Nam, W.; Que, L., Jr.; Stubna, A. *J. Am. Chem. Soc.* **2008**, *130*, 12394−12407.


DOI: 10.1021/jacs.6b07708
*J. Am. Chem. Soc.* 2016, 138, 14312−14325

(45) Malrieu, J. P.; Guihéry, N.; Calzado, C. J.; Angeli, C. *J. Comput. Chem.* **2007**, *28*, 35−50.
(46) Pierloot, K. *Mol. Phys.* **2003**, *101*, 2083−2094.
(47) Neese, F.; Petrenko, T.; Ganyushin, D.; Olbrich, G. *Coord. Chem. Rev.* **2007**, *251*, 288−327.
(48) (a) Van der Avoird, A.; Ros, P. *Theor. Chim. Acta* **1966**, *4*, 13−21. (b) Desjardins, S. R.; Penfield, K. W.; Cohen, S. L.; Musselman, R. L.; Solomon, E. I. *J. Am. Chem. Soc.* **1983**, *105*, 4590−4603.
(49) McWeeny, R. *Methods of Molecular Quantum Mechanics*; Academic Press: San Diego, CA, 2001; p 379.
(50) Ye, S.; Neese, F. *Inorg. Chem.* **2010**, *49*, 772−774.


DOI: 10.1021/jacs.6b07708
*J. Am. Chem. Soc.* 2016, 138, 14312−14325